Yonas Tadesse[1]
Department of Mechanical Engineering,
Center for Energy Harvesting Materials and Systems (CEHMS),
and Center for Intelligent Material Systems and Structure (CIMSS),
Virginia Tech,
Blacksburg, VA 24061
e-mail: yonas@vt.edu

Dennis Hong
Department of Mechanical Engineering,
Robotics and Mechanism Laboratory (RoMeLa),
Virginia Tech,
Blacksburg, VA 24061
e-mail: dhong@vt.edu

Shashank Priya
Department of Mechanical Engineering,
Center for Energy Harvesting Materials and Systems (CEHMS),
and Center for Intelligent Material Systems and Structure (CIMSS),
Virginia Tech,
Blacksburg, VA 24061
e-mail: spriya@vt.edu

Twelve Degree of Freedom Baby Humanoid Head Using Shape Memory Alloy Actuators

A biped mountable robotic baby head was developed using a combination of Biometal fiber and Flexinol shape memory alloy actuators (SMAs). SMAs were embedded in the skull and connected to the elastomeric skin at control points. An engineered architecture of the skull was fabricated, which incorporates all the SMA wires with 35 routine pulleys, two firewire complementary metal-oxide semiconductor cameras that serve as eyes, and a battery powered microcontroller base driving circuit with a total dimension of 140 $\times 90 \times 110$ mm^3. The driving circuit was designed such that it can be easily integrated with a biped and allows programming in real-time. This 12DOF head was mounted on the body of a 21DOF miniature bipedal robot, resulting in a humanoid robot with a total of 33DOFs. Characterization results on the face and associated design issues are described, which provides a pathway for developing a humanlike facial anatomy using wire-based muscles. Numerical simulation based on SIMULINK was conducted to assess the performance of the prototypic robotic face, mainly focusing on the jaw movement. The nonlinear dynamics model along with governing equations for SMA actuators containing transcendental and switching functions was solved numerically and a generalized SIMULINK model was developed. Issues related to the integration of the robotic head with a biped are discussed using the kinematic model. [DOI: 10.1115/1.4003005]

Keywords: humanoid, facial expression, artificial skin, shape memory alloy

1 Introduction

Small biped humanoid robots that can perform several household actions are increasingly becoming the focus of research. The design of humanoid head for a given platform is a challenge and requires an assessment of various factors including the overall size of the artificial skull, the choice of appropriate actuator, artificial skin, actuation points on the face, sequential control of anchor lines, driving electronics, and low power consuming programmable microprocessor. This comprehensive study describes the development of a small scale baby humanoid robot including the architecture of the head with structural and computational modeling, analysis on the selection of appropriate musclelike actuator, driving electronics for battery powered operation, dynamic modeling and characterization for achieving a wide range of expressions, and overall appearance in relation to the size of the head for gesture synthesis and stability issues. There are many potential applications for small scale baby robot including child education, entertainment, and medical studies. Baby robots will further help in understanding the human anatomy and provide support to the ongoing research in prosthesis. Another important aspect in the development of a facial expressive humanoid robot is to bring machinelike structures having a resemblance to that of humans. This will allow us to bridge the gap between the machine world and human world.

This paper is organized in 11 sections. First, we introduce the background and the actuator selection criterion for small scale robot head. A thorough comparative analysis is presented, covering most of the prominent artificial muscle candidates. Second, a literature survey is presented on facial expressive humanoid prototypes. Third, the architecture of small baby robot head will be presented focusing on the computer-aided design (CAD) model, structural and fabrication issues, configuration of action unit, and layout of all the mechanical and active elements within the distorted volume. Fourth, a brief discussion is presented on driving electronics and control sequence of facial actions. Fifth, results from the experimental characterization of prominent facial movements such as cheek movement, jaw, and gesture synthesis on a biped platform are discussed. Sixth, the dynamic modeling of head focusing on jaw movement and typical configuration of skin-SMA actuator will be discussed. Sections 7–9 cover the SIMULINK and numerical modeling of system dynamics based on SMA actuation. In Sec. 10, we validate the models using the experimental results and summarize the findings in Sec. 11 of this paper.

For the design and development of facial expressive baby robot as tall as 600 mm, a head with overall outside dimensions of 140 mm height, 90 mm width, and 110 mm depth is a good choice. However, these metrics are challenging because of the limited space available to accommodate various actuation, mechanical, and electrical components. The use of servo motor based actuator is ruled out as it does not provide physical resemblance to human facial anatomy, consumes large amount of space and power, produces noise and heat, and requires additional mounting assembly. Rather, the focus was on musclelike actuators, which mimic the resemblance and performance of human muscles. Contractile types of actuators such as SMAs are appropriate choice for facial artificial muscles. SMA actuators require simple current drive, the overall size is small ($\sim$100 μm in diameter), and provide strain up to 4% in real conditions with blocking stress greater than 200 MPa [1]. The high power to mass ratio of SMAs is advantageous in scaling the total size and weight of the humanoid head. SMA actuators do not generate acoustic and electromagnetic noise that might interfere with voice recognition system and drive electronics. Further, SMAs are commercially available in large quantities, exhibiting a repeatable performance.

Figure 1 compares the blocking stress, strain, and electrical power requirements of prominent artificial muscle candidates with that of human facial muscles. Four actuator technologies, which

[1]Corresponding author.

Contributed by the Mechanisms and Robotics Committee of ASME for publication in the JOURNAL OF MECHANISMS AND ROBOTICS. Manuscript received January 19, 2010; final manuscript received October 1, 2010; published online January 10, 2011. Assoc. Editor: Jean-Pierre Merlet.

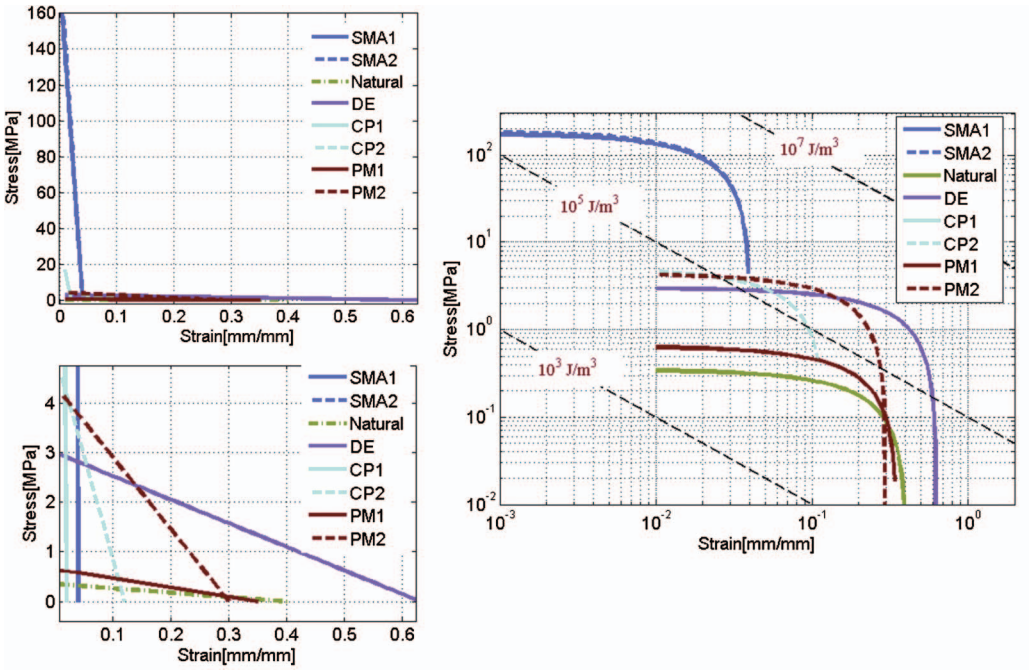

Fig. 1 Blocking stress-strain relationship of actuator technologies for humanoid face. (*a*) Wide range stress, (*b*) inset of lower stress, and (*c*) logarithmic plot. CP=conducting polymer, SMA=shape memory alloy, DE=dielectric elastomer, and PM =pneumatic muscle.

are promising candidates for facial expressive humanoid head, are presented in this table. The performance of actuators can be compared in terms of blocking force and free strain. Ignoring the hysteresis loop for forward and backward actuations, the relationship between the blocking stress and free strain can be expressed by a linear line with a negative slope represented as

$$\sigma = -\frac{\sigma_b}{\varepsilon_f}\varepsilon + \sigma_b \tag{1}$$

where σ is the stress generated by the actuator, σ_b is the blocking stress that the actuator can produce at zero displacement, ε_f is the free strain of the actuator when no external load or constraint is applied on it, and ε is the strain at a given stress. Equation (1) can be used to compare the performance of various low profile actuator technologies and geometry, as shown in Table 1.

The blocking stress and strain diagrams for different types of actuation technologies are shown in Figs. 1(*a*)–1(*c*). Figures 1(*a*) and 1(*b*) show the linear expressions presented in Table 1, and Fig. 1(*c*) illustrates a logarithmic plot of the same expressions. The actuation performance metric is represented as a curved line and the plot presented in Fig. 1(*c*) is helpful in identifying the suitable muscle for facial robotics. The voltage applied to dielec-

Table 1 Stress-strain relationship for low profile actuator technologies

Actuator type	Blocking stress-strain equation	Comment
Shape memory alloy	(a) $\sigma=-4.7\times10^3\varepsilon+1.9\times10^2$; (b) $\sigma=-4.5\times10^3\varepsilon+1.8\times10^2$	Current consumption is 180 mA at an applied field of 27 V/m. Equation (a) is for 100 μm diameter wire and equation (b) is for 127 μm diameter wire [2].
Dielectric elastomer	$\sigma=-4.8\varepsilon+3\times10^0$	Dielectric elastomer, though, provides high practical strains up to 63%; the required electric field is too high of the order of 110–350 MV/m. A 150 μm thick diaphragm requires about 190–300 V [3–6].
Conducting polymer	(a) $\sigma=-1.7\times10^3\varepsilon+3.4\times10^1$; (b) $\sigma=-4.2\times10^1\varepsilon+5\times10^0$	Polypyrrole actuator is promising as it requires small power <100 mW. Typical strain is between 2% and 12% and stress is in the range of 5–35 MPa. Equation (a) is for 34 MPa and 2% strain and Eq. (b) is for 5 MPa and 12% strain [3,6,7].
Pneumatic	(a) $\sigma=-1.9\times10^0\varepsilon+6.5\times10^{-1}$; (b) $\sigma=-14.5\times10^0\varepsilon+4.4\times10^0$	(i) Extended actuator length is 1780 mm with a contracted diameter of 70 mm, an exhibiting force of 2500 N, and a strain of 35% [8]; (ii) Braided pneumatic muscle having a length of 614 mm and an outside diameter of 14.3 mm; the diameter of one strand is 25 mm, the number of strand is 240, the length of one strand is 650 mm, and the spiral number is 4.7 [8,9]. Equation (a) is for 500 kPa and equation (b) is for 300 kPa. Power requirement of pneumatic actuator is usually high because it is driven by a bulky compressor that also requires electrically activated solenoid valve.
Natural muscle	$\sigma=-8.7\times10^{-1}\varepsilon+3.5\times10^{-1}$	Assuming natural muscle as a linear actuator [3,4].

tric elastomer is in the thickness direction of actuator and usually the thicknesses are in micrometer range. Thus, the total voltage required is quite large. For example, a 10 μm thick membrane generally requires voltage in the range of 1 kV. The total volume of the actuator is also large since it requires a prestretching mechanism to operate. SMA actuator power consumption is often specified in terms of the length of the actuator. For example, a 100 μm in diameter and 100 mm long SMA wire will require voltage in the range of 2.7 V/50 mA. Pneumatic actuators are difficult to compare because they require several peripheral elements to operate, but the overall power requirement is quite high.

From these figures, it can be seen that SMAs are appropriate actuator technologies in humanoid face as they require moderate power and provide enough strain and force. SMA actuators have certain advantages as compared with that of conventional actuators, namely, (i) low overall profile typically in micrometer size diameter, (ii) provide the highest force to weight ratio, (iii) use simple current drive, and (iv) operation is silent. In spite of these advantages, SMA actuators have a limited application due to their low operational frequency and narrow bandwidth. The bandwidth is limited due to the time required to undergo the phase transformation. The response time of SMA actuator is also dependent on preloading stress, loading condition, and amplitude of activation potential. We have characterized the actuator performance of commercially available nickel-titanium (NiTi) based shape memory alloy actuators, Flexinol (FL, Dynalloy, Inc., Tustin, CA), and Biometal fiber (BMF, Toki Corporation, Tokyo, Japan). It was found that for equal diameter of Flexinol and Biometal fiber, the Biometal fiber cools faster than the Flexinol. Flexinol force generation rate was of the order of 1–7 MPa/s in the prestress range of 0–160 MPa, whereas for Biometal fiber, the force generation rate was 10–80 MPa/s in the prestress range of 0–320 MPa [10]. One of the clear differences between the two SMA actuators (Flexinol and Biometal) is their flexibility wherein Biometal fiber is more flexible. Thus, Biometal fiber was selected in this study as compared with Flexinol. Biometal fiber is commercially available from Toki Corporation [11].

In order to produce complex facial expressions, a deformable elastomeric skin with selected control points should be sequentially actuated. If a contractile type of actuator is utilized to drive the control points, the sinking points (or the terminating points) of the actuator on the skull should be selected. The sinking point determines the magnitude of facial deformation as well as the direction of action depending upon the configuration of the artificial muscle. It has been demonstrated in the literature that control points (action units) on the face are close to the facial features such as tip of the mouth, nose, edge of cheek muscle, and frontal eyebrow [12–14].

2 Facial Expressive Humanoid Prototypes

There are 268 voluntary muscles that are responsible for creating facial expression. Three primary muscle types are (i) linear muscles that share common anchor points, (2) sheet muscles that run parallel to each other and are activated together, and (iii) sphincter muscles that contract at center point [15,16]. To replicate all the voluntary muscles on the facial expressive humanoid is a challenging issue and none of the humanoid heads developed so far duplicate all the facial muscle of the biological head.

In the area of computational biology and psychology, facial action coding system (FACS) was proposed by Ekman and Friesan in 1978, which provides a correlation between facial deformation and the muscles involved. FACS defines 46 action units related to the anchor points pertaining to expression-related muscles [17]. An additional 20 action units for gross head movements and eye gazes were identified. FACS was implemented on graphical work station and is being used in the development of talking head for animations and video games. The implementation of FACS in humanoid faces is dependent on the platform of choice and requires progress in hardware with smart architectures.

Some of the famous prototypes in the world developed to study cognitive sciences are Albert HUBO [12,18], SAYA [19], Replee Q1 and Q2 [20], Robota [21], and ROMAN [22], where emphasis has been on the external skin and achieving a physical appearance akin to that of human being. Albert-Hubo utilizes the servo motor for face actuation with large array of facial motion capability (39DOFs) [12,18]. Lilly is also a servo motor based facial robot with embedded piezoelectric sensors in the facial skin focusing more on the human-robot interaction (16DOFs) [23]. SAYA head utilizes Mckibben actuators (19DOFs) [19]. The pneumatic muscle introduced in SAYA was believed to improve the structural appearance of the face. Repliee Q1 (31DOFs) and Q2 (42DOFs) are both full body humanoid robot with a capability to express articulated facial and hand motions using pneumatic actuators [20]. Several functions using humanoids have been demonstrated such as flute playing [24], receptionist [25,26], and patient care [27]. These prototypes have also been used in testing the theory of uncanny valley [28–30], interaction ability, and social aspects [31].

A detailed description of the challenges in developing the facial expressive humanoid head with dc motor, shape memory alloy, and McKibben has been provided by Kobayashi et al. [32,33]. Three generations of heads were presented in that study and the first generation was 1.5 times bigger than the human-size head and actuated by a pressurized air cylinder. They were able to build a prototype of human-size head with McKibben actuator. This study pointed out that the humanlike skin and the selection of action units on the face are critical in achieving a realistic facial expression. The action units for a prototype face could be adapted from the FACS.

SMA actuator has been previously used for the human-size head with 210 mm height and 2.1 kg weight [34]. An improved version of robotic human head was reported by Hashimoto et al., which utilizes McKibben pneumatic actuators along with coil spring mechanism for head motion [19]. A number of realistic facial expressions and humanlike movements were demonstrated. A piezoelectric motor based humanoid face has also been reported [35], which had the drawback of complex driving circuit and position feedback. The application of dielectric elastomer for artificial facial muscle has been presented by Rossi et al. [36]. A humanoid face with "face film" as a skin and low friction driving mechanism for action units was presented in Ref. [13]. The face film utilized in this study was analogous to the elastomeric skin often used in humanoid heads. The low friction pulling mechanism used a rope that was guided within a tube sliding over spring coil. This mechanism was found to be suitable for attachment with skin.

A small humanoid robot that could be used for disabled children education was reported by Guenter et al. [21]. This study emphasized the mechanics of upper body and presented the design for 23DOFs, including a three DOF spine, a seven DOF arms, a three DOF pair of eyes, and a three DOF neck. Currently available commercial baby humanoid robots do not have expressive face. The majority of these robots have emphasis on locomotion, which is attractive for children. However, a combination of fully expressive face with biped will allow us to fully exploit the capability of humanoids in household applications such as tutoring children.

3 Shape Memory Alloy Actuated Humanoid Head Architecture

3.1 Baby Face Skull CAD Model. A baby doll was selected as the model for fabricating the robotic head. The model was scanned using laser scanner (Cyberware 3030 RGB/MS) from which a three-dimensional solid meshed geometry was obtained, which can be exported to CAD software such as SOLID WORKS. Mechanical features were created in the CAD model by constructing several auxiliary planes to generate physical effects such as jaw, eye opening, and teeth and also producing a hollow section in the skull by revolving a cutout so that mechanical elements can be

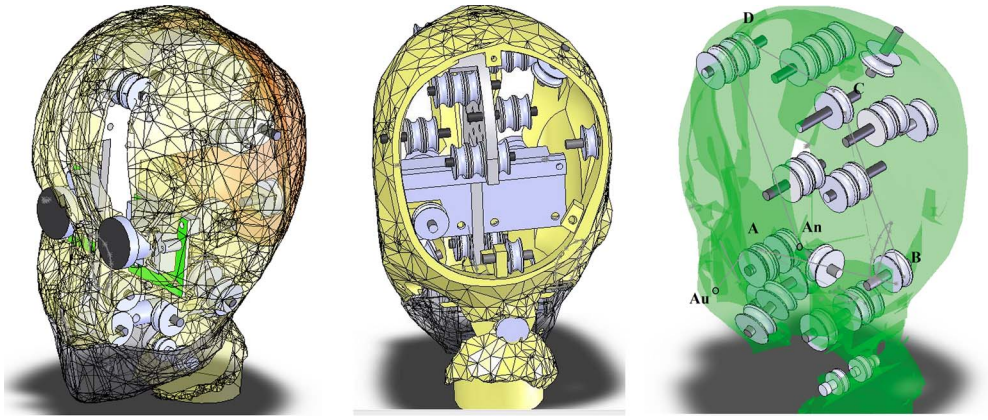

(*a*) (*b*) (*c*)

Fig. 2 CAD design of robotic head. (*a*) Isometric view of CAD (front), (*b*) rear isometric view, and (*c*) SMA actuators and a pulley system. (Note: skin layer is not shown in this figure.)

mounted. As shown in Fig. 2, the head encompasses a structure, which houses 35 pulleys each of 12 mm outer diameter and 5 mm thickness made from zinc plated steel, a perforated midplate for SMA routing lines, a 3DOF neck mechanism, and a stationary firewire complementary metal-oxide semiconductor (CMOS) camera for vision system. The outside of the skull structure was covered by the elastomeric silicone skin. Details on the fabrication and optimization of skin material can be found elsewhere [37]. Nine actuation units (AUs) on the face and a separate jaw actuation were employed for the demonstration of facial expression. The number of actuation points was limited by the available space inside the skull. The space had constrains on SMA wires, which needed to be routed inside the skull without touching each other. One end of each SMA actuator was attached to the action unit and the other end was secured to the skull structure after passing through a series of pulley system. Therefore, the total degree of freedom of the modular head, which includes the skin actuation and neck motion was 12 (12DOF)s. The third degree of freedom of the neck was activated by the servo motor mounted on the shoulder of the miniature humanoid robot. The SMA actuators were controlled by a custom-built microcontroller based driver circuit, which can control 16 SMA actuators by enabling the microcontroller output port. The development process of the baby head from the CAD model to the prototype is shown in Fig. 2 in a more descriptive way. Figures 2(*a*) and 2(*b*) illustrate the topology of the pulley system in 3D space within the skull and their arrangement from the front isometric and rear point of view. It can be seen that pulleys are distributed within the midplane and also on the side-wall of the skull. One advantage of using the pulley system configuration is that it allows replacement of SMA actuator if any damage occurs. Figure 2(*c*) shows the typical SMA actuator (solid dark line) passing over several pulleys with its two ends points ("Au" and "An"). Au is an attachment point to the skin (moveable when SMA is actuated) and An is an anchored point at the back of the head (fixed point).

3.2 Prototyping and Hardware Elements. The skull is the basic structure that keeps the skin (the morphing shape) in its neutral position. We found that a full solid skull structure does not provide a humanlike facial movement. A supporting skull structure adapting the skeleton of natural human skull guides the directional movement of skin material and provides better performance. The prototype skull structure is shown in Fig. 3, which consists of sectioned solid material that reduces friction between the skin layer and the skull. The head structure should have low mass and moment of inertia for efficient neck motion and therefore rapid prototyping fabrication method with sparse configuration rather than dense solid was used. As can be seen in Fig. 3(*a*), the curved surface of the prototype has polygonal elements, which will increase the surface roughness of the skull and therefore require large force to pull the skin. The actuation behavior of the skin is dependent on the attachment between the skin and the skull. The portion of skull, which directly contacts with the skin, was removed in order to reduce the force required by SMA actuators, as shown in Fig. 3(*b*).

The vision of the robotic head consisted of firewire camera installed within the skull. The choice of firewire camera with on board processor helps in processing the images and visual perception rapidly. Firewire (IEEE 1394) communication scheme provides the fastest transmission of data and allows a quick response for external environmental interactions. Figure 4 illustrates a modular picture of stereo eye system. The eye mechanism is not

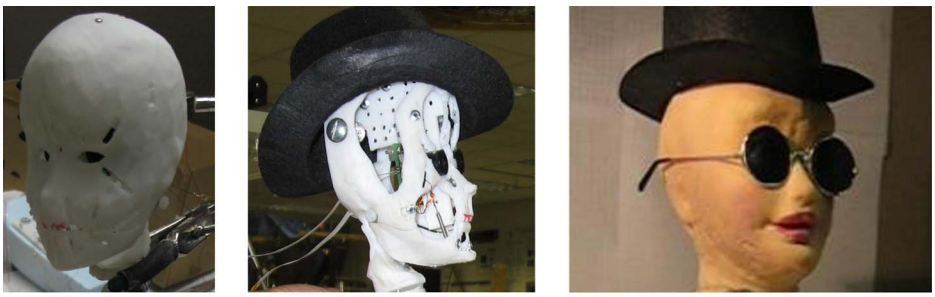

(*a*) (*b*) (*c*)

Fig. 3 Pictures of prototype robotic head development. (*a*) Prototype solid support structure, (*b*) modified natural looking skull structure, and (*c*) elastomeric skin with the skull.

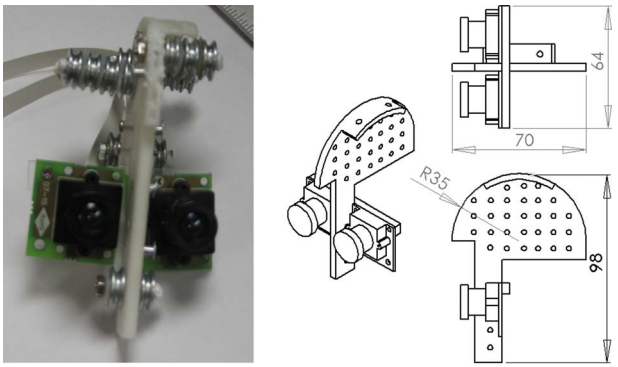

(*a*) (*b*)

Fig. 4 Vision system. (*a*) Pictures of the vision system of the head. (*b*) CAD drawing.

unique for this design but intended to provide capability for reconstruction of images in 3D perception. It is to be noted that there is some trade-off between developing high degree of freedom facial movement on a very small scale and embellishing all features of biological facial emotion.

The skin material was synthesized from the commercial platinum cured silicone elastomeric material composed of mainly polyorganosiloxanes, amorphous silica, platinum-siloxane complex compound, foaming agents comprising of sodium bicarbonate, diluted form of acetic acid, and silicone thinner. The mixture with foaming agents was casted within a polyurethane mold. The stiffness characteristics of each facial action unit was done by mounting the skull-skin assembly on translating stage with force transducer attached at the end of a fishing wire, which was then connected to the respective anchor points. The picture of the experimental setup is shown in Fig. 5(*a*) and the schematic diagram describing the characterization technique is shown in Fig. 5(*b*). The testing was done by translating the linear stage by a distance that is equal in magnitude to that of facial deformation and measuring the force required to create the translation. The force sensor was calibrated beforehand and the voltage output (V_{sen}) was converted into the corresponding force (F_s) using the expression (F_s=972.06 V_{sen}+146.78). It can be seen in Fig. 5(*c*) that the force requirements are below 2.5 N (250 gm) force. The highest force was required for the movement of the jaw.

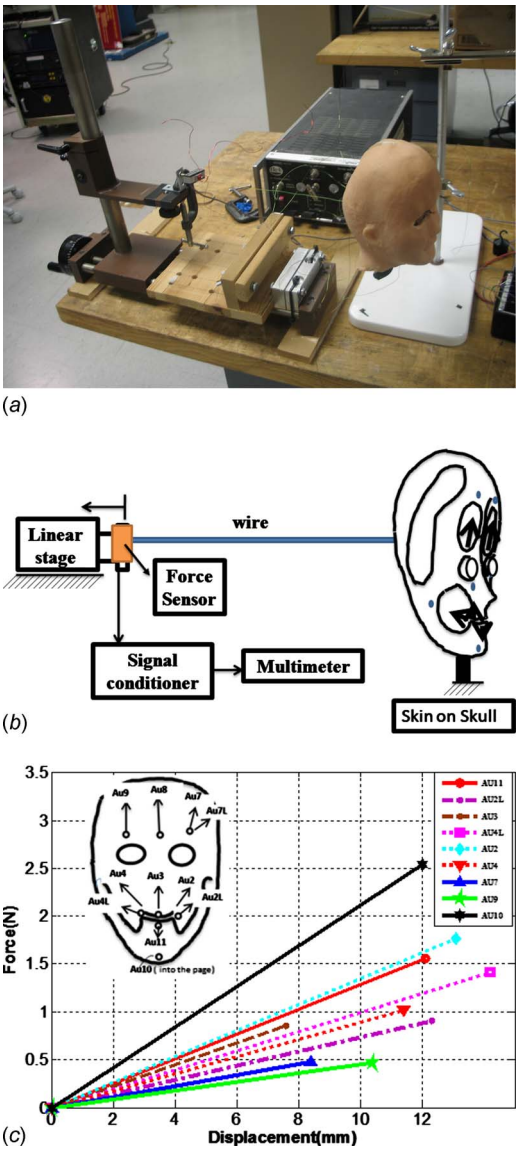

(*a*) (*b*) (*c*)

Fig. 5 Skin stiffness characterization. (*a*) Picture of the experimental setup, (*b*) schematic diagram of the experimental setup, and (*c*) force versus displacement diagram for the synthesized skin along the deformation lines shown in the inset.

3.3 Action Units and Actuator Configuration. Based on FACS and by observing the feature points on the face, the action units were selected, as shown in Fig. 6. In our small prototypic head, ten AUs were used including the jaw movement. In Fig. 6, the origin and direction of action units are indicated. The length of the SMA wire, which is rerouted around the pulley within the skull, type of SMA, number of SMA at each action unit, and the wire resistance of SMAs at action units are tabulated in Table 2. These values determine the facial deformation of the face as the SMA only provides a practical strain of 4%. The last entity is the type of SMA actuators utilized where FL stands for Flexinol and BMF stands for Biometal fiber. Initially, we used a combination of Flexinol and Biometal fiber actuators in the face by distributing the BMF in fast moving areas and the Flexinol in other areas since BMF is relatively expensive than Flexinol. This was also done so that one can simultaneously conduct a comparative study on these two SMAs.

The location of AUs or control points was chosen for basic emotional demonstration, which happens to be few control points. Since the size of the skull is the same as that of a normal palm, there is a serious space constraint which limits the number of actuation points. Figure 6 illustrates the actuation points and their direction on the frontal plane. The AUs are listed in Table 2. The other parameters in this table are the number of actuators at each action unit, the length, and the type of actuator used. The neck used the servo motors to implement a parallel chain driven on the ball and socket joint pivoting about an axis. The head was balanced by four springs, which were tightened to hold the head in an equilibrium position. This mechanism helps the head to be stable at all times and requires less driving torque.

The effect of the number of actuators on force and displacement when connected in a parallel configuration can be determined by measuring the deformation for each action unit. It is known that SMA actuator exhibits nonlinearity; however, this behavior can be ignored since the applied currents are below the critical level.

Considering Fig. 7(*a*) for one SMA actuator with blocking force F_b and practical free strain ε_f, the relationship can be expressed by a linear line with negative slope. If two SMA actuators of the same length are used together, the force will be amplified by two times and the strain will remain the same. Therefore, force gets amplified by the number of SMAs attached at a particular point. The skin characteristic curve is a positive slope line. The action unit can be connected to a number of shape memory alloy actuators with each action unit having its own unique displacement

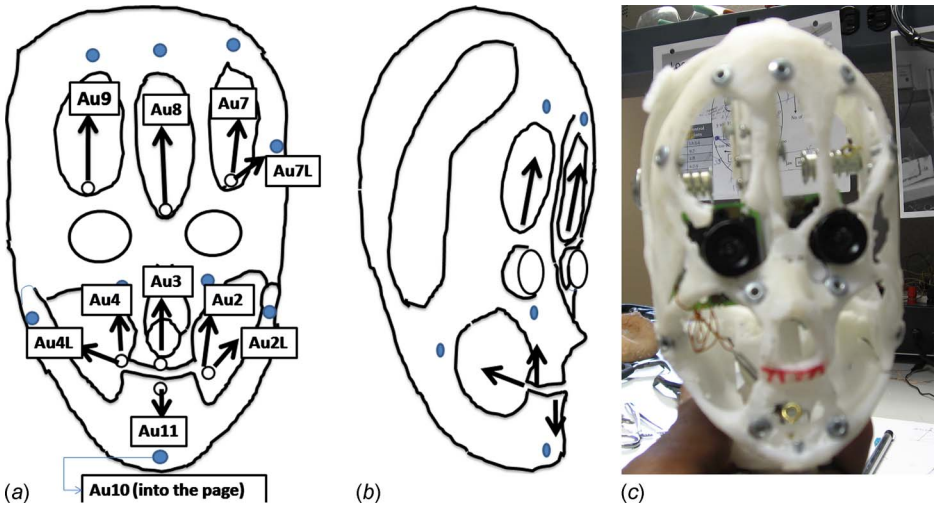

Fig. 6 Action unit and direction of movement on the skull. Schematic diagram in (*a*) frontal view, (*b*) side view, and (*c*) frontal view of the actual prototype, in pictorial view.

characteristics because the thickness of the skin at each action unit could be slightly different, which results in force anisotropy. Therefore, it was important to study the force and displacement relationship rather than the stress-strain relationship.

Figure 7(*a*) demonstrates the shape memory actuator force displacement characteristics. The governing equation for multiple SMA actuators connected at an action unit can be considered as a linear line

$$F = iF_b\left(\frac{D}{\varepsilon_f} + 1\right) \tag{2}$$

Here, F is the actuator force, F_b is the blocking force of SMA, i is the number of actuators with the same diameter, D is the displacement, and ε_f is the free strain. The load line could be variable across the face of the robot and it can be determined experimentally. This relationship can be represented as

$$F = m_v D \tag{3}$$

where F is the force and m_v is the slope of the skin characteristic (determined experimentally). The operating point of the action unit on the face can be determined by the intersection of Eqs. (2) and (3) given as

$$D_{oi} = (iF_b)\left(\frac{iF_b}{\varepsilon_f} + m_v\right)^{-1} \tag{4}$$

Equation (4) depicts how the operation point, which is the point of interest of an action unit, is displacing under different configurations of SMA arrangement at an action unit. The blue dashed line in Fig. 7(*b*) indicates the force and displacement characteristics of each action unit measured experimentally. The intersection of the actuator line and load characteristic curve provides the operating point of a particular action unit. For example, for jaw movement (AU10) shown in Fig. 7(*g*) and 7(*m*), one Flexinol actuator (blue) line can provide a mouth opening of 5.5 mm, two SMAs (green line) can provide 7.5 mm, and three SMAs (purple line) can provide 8.5 mm. In comparison, one Biometal fiber (blue) line can provide a mouth opening of 7 mm, two can provide 9 mm, and three can provide (purple line) 10 mm. Using several SMA actuators might not be desirable because due to heat dissipation and high power consumption, there is a practical trade-off. A comparative plot of skin-actuator relationships for Flexinol and BMF with respect to each action lines was taken into consideration. The left side in Fig. 7 represents the data for Flexinol actuator and the right side for Biometal fiber actuator. The force and displacement axis of each plot were made to be the same to indicate that there exists a variation of force-displacement characteristics during actuation of the skin. Such behavior is related to the variable thickness of the skin, the roughness of supporting structure, and the existence of support structure around action unit. The blocking stress of Biometal fiber actuator is 500 MPa. The vendor for Biometal fiber actuator lists the performance of the actuator in terms of practical force produced at optimum driving conditions in order to indicate the useful kinetic force available [11]. The maximum pulling force of a 127 μm (0.005 in.) Flexinol wire is 2.25 N (230 gm) as provided by the manufacturer, Dynalloy Inc., Tustin, CA [2].

Table 2 Actuator parameter used on the face

Name of action unit	Length (mm)	No. of actuators	Measured resistance (Ω)
Au-2	265	2 BMF	19.2
Au-2L	265	2BMF	17.8
Au-3	230	1 BMF	31.5
Au-4L	220	2 BMF	14.8
Au-7	275	2FL	19.3
Au-7L	150	1FL	10.5
Au-8	360	2FL	12.6
Au-9	255	2FL	8.9
Au-10	275	4BMF	8.4
Au-11	270	2BMF	18.2

3.4 Integration Issues. After synthesizing the skin, control points on the inside part of the skin were selected according to FACS [17]. First, the mechanical support structure system was assembled and then the skin was attached to SMA actuators at the action units. Next, the skin and SMA assembly were mounted on the skull, having feature points, which exactly fitted the section created on the skull. The challenge of packaging the baby head is to reroute the SMA wire without touching each other within the skull compartment and keeping the outer skin in a consistent geometrical arrangement. Another aspect is the heat generation within the compartment, which needs to be removed to effectively actuate the face. To this end, the back side of the skull cover was made to be perforated. A forced convection system might be considered to excavate the heat inside. Figures 8(*a*)–8(*c*) illustrate the front face, inside of the skull, and assembled head from the back side. One end of each SMA actuator was connected to the skin with a ring terminal hooked inside the skin so that it will not be visible from the outside part of skin. The SMA actuators then passed

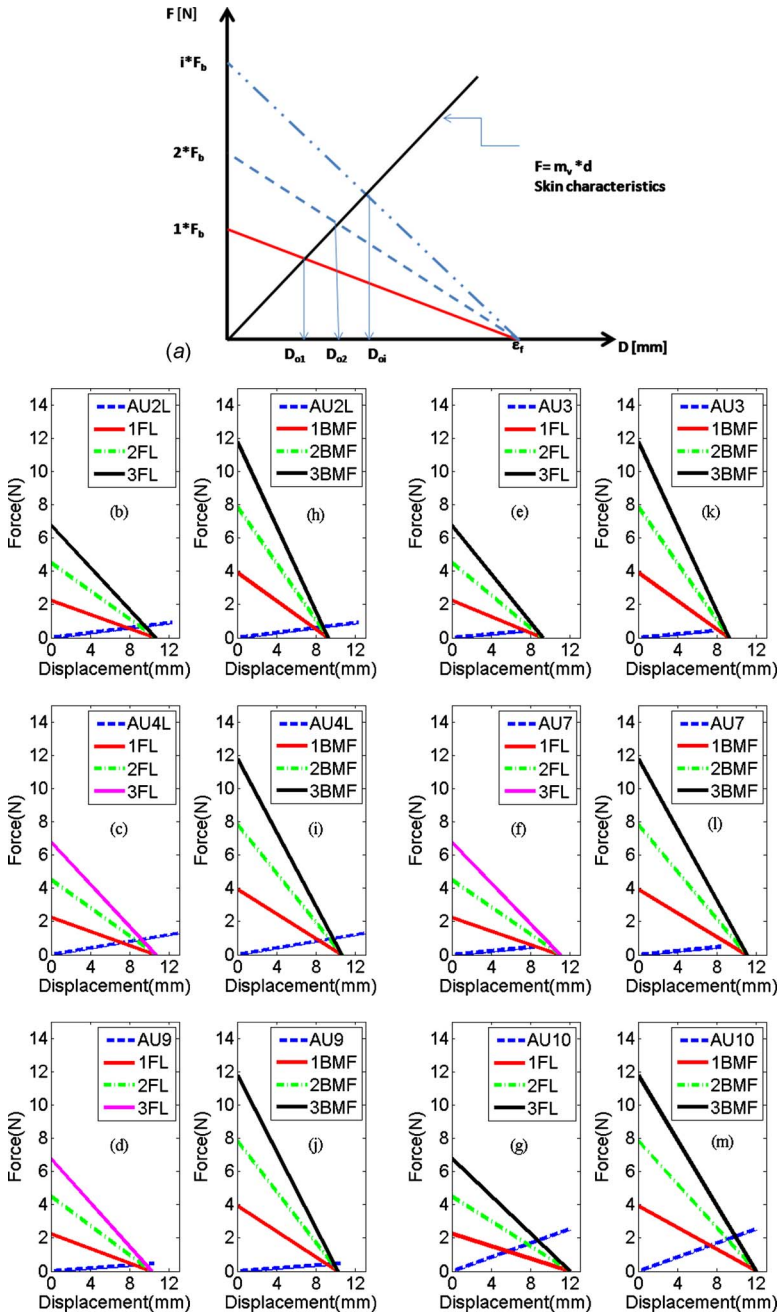

Fig. 7 SMA actuator-skin deformation relationships. (*a*) Generalized actuation characteristics, (*b*)–(*g*) Comparative force-displacement characteristics of AUs utilizing Flexinol wire (127 μm wire), and (*h*)–(*m*) Biometal fiber (100 μm wire) in parallel configuration.

through the sinking points on the skull, rerouted on the pulleys inside the skull, and finally anchored on the other end. The prototype presented in this paper illustrates all the issues of developing a small scale biped mountable baby robot head. For mass production of heads, the attachment points on the skin need to be allocated precisely in the molding process of the skin and the assembly of the skin, actuators, and the skull needs to be automated.

4 Driving Electronics and Control

The integration of hardware and software for robotic system requires the implementation of a microcontroller or microprocessor based system to incorporate a preprogramed sequence of commands and also a real-time decision making. The application of microcontroller based circuits has been demonstrated on various robotic platforms such as actuator arrays [38,39], jellyfish inspired unmanned underwater vehicle [40], climbing robots [41], mobile robots [42], robot localization [43], and automatic guidance [44,45]. Building upon this prior information, the basic constituents of the driver system implemented in the head included a microcontroller, amplifier chip, voltage regulator, and other passive circuit elements. PIC 16 series microcontroller (16F874) was used for programming and interface. Peripheral interface controller (PIC) is a CMOS flash-based 8 bit microcontroller with electrically erasable programmable read-only memory (EEPROM), 40 pins, and four ports that can be configured as input and output. It has three internal timers that can be used to generate real-time interrupt routines. The principle of operation for the developed

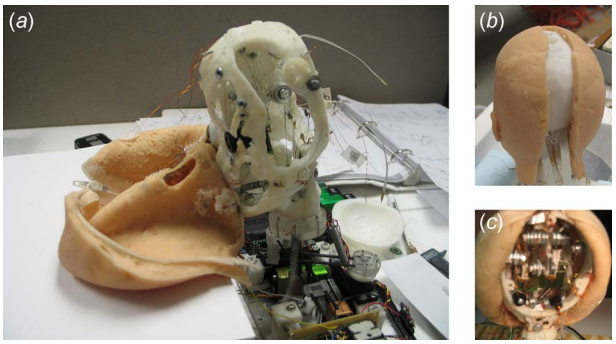

Fig. 8 (*a*) Skin-skull-actuator assembly, (*b*) back side of the head with a slot created in the skin to gain access inside the head, which can be sealed using zipper, and (*c*) inside of the head after completing the assembly

driving circuit is as follows. The microcontroller sends signal to the enabling port of the current amplifier chip. A transistor-transistor logic TTL high is connected to the other ports of the amplifier chip and makes the logic input to be "true" all the time. The sequential driving of SMA actuators attached to the output terminal of the current driver chip is done by providing a wavelet type signal by programming the microcontroller. The controller utilizes a 20 MHz crystal oscillator. One of the ports of the microcontroller was configured to be as input and attached to the external switch. The external switch was made in such a way that it can be set manually or it can be triggered from the main processor of the biped torso. This enables to test the robotic head on a separate table top or by mounting the head assembly onto a biped robot. The microprocessor requires external support hardware such as external RAM, ROM, and peripherals, whereas the microcontroller needs very little external support hardware as the RAM, ROM, and peripherals are built on the chip. The programming of microcontroller was done in assembly language using MPLAB IDE (Integrated Development Environment) and development board PICDEM™ 2 PLUS. The sequencing of port activation was done by calling a delay loop. First, a delay loop routine was written for 1 s and the output ports, port B and port C, were configured as Tristate. The ports were activated by setting them high using bit clear file (BCF) and resetting with bit set file (BSF) instruction sets and calling the delay in between these commands. The advantage of using assembly language is that very few instruction sets for the controller are required, which increases the efficiency and memory space utilization.

Figure 9 shows the schematic diagram of the circuit. In this figure, manual trigger, power supply to the digital logic input, clock, and driver module are shown as dashed lines. The manual control module includes a master clear (MC) and an activation push button (AB), which are used to test the facial activation code downloaded to the microcontroller. Master clear was used to reset the program and the activation button was used to trigger the facial expression routine code during table top testing. Once the AB is triggered, the microcontroller can trigger the driver module autonomously, depending on the code embedded in the microcontroller, which in turn activates the corresponding set of SMA actuators. In the case of biped mounted head, the activation button can be turned on by the main processor of the robot.

The typical sequence of actuation of each action unit is shown in Fig. 9(*b*). The measurement was done for an open loop terminal voltage using National instrument (NI 2121) data acquisition card with eight channel analog input. For example, in Fig. 9(*b*), AU8 and AU3 are activated at the same time for 2 s for demonstrating a "surprise" type of expression, while AU2 and AU4 are activated together for mild smile. The pulse train presented in Fig. 9(*b*) is one subroutine executed for 50 s facial activation implementation. The delay between each sequence, the activation time, and the simultaneous engagement of action units determine the facial emotion of the prototype face. Therefore, it is important to adjust these parameters during programming the microcontroller. The characteristic of the current amplifier L298 chip was measured by sweeping a constant resistance and recording the voltage and current simultaneously. The resistance value was chosen in the range of resistance of shape memory alloy actuators. Chips A and B get the voltage and current characteristics from a 5 V regulator 8705 chip, which limits the voltage below 5 V. Chip C represents the current and voltage of a dc power battery source directly attached to the amplifier chip. This configuration helps in studying the behavior of the circuit under different circumstances. It should be noted here that an adjustable potentiometer driving circuitry is required to control the exact magnitude of voltage and current. All the circuit components were vertically stacked on the board. The

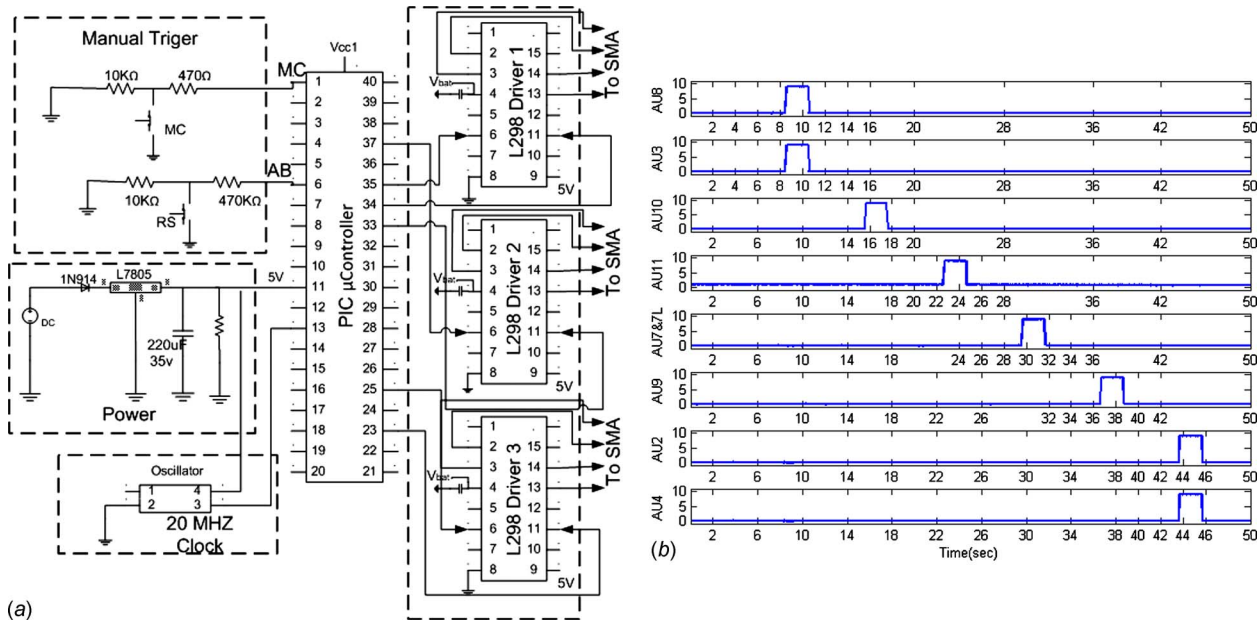

Fig. 9 (*a*) Schematic diagram of the driving circuit for the SMA head. (*b*) Sequence of facial activation for 1 cycle.

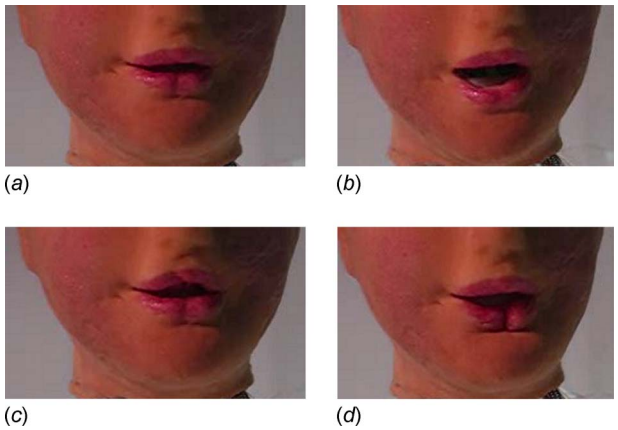

Fig. 10 Facial expression around the mouth, (*a*) lips normal position, (*b*) mouth open by lower jaw movement, (*c*) upper lip protruded outward, and (*d*) lower lip pulled inwards

servo motors used in neck mechanism were controlled by using a commercially available Polulo controller with a USB interface. The head was balanced by four springs, which were tightened to hold in equilibrium position. This mechanism helps the head to be stable at all times and reduces the driving torque of the motor during actuation.

5 Face Characterization

Facial expressions were characterized by recording a series of video sequences. The face deformation can be recognized by visualizing the marked points on the face in the area where action unit was deployed. The first characterizations were performed near the mouth area. Figures 10(*a*)–10(*d*) show the normal position, jaw opening, upper lip moving upward, and lower lip drawn inwards. The deformations on the face are mainly dependent on the attachment points and the movement direction of the actuators.

Representative smiling was measured by gluing a black circular disk on the tip of the lip and tracking the movement from video recording synchronously sampled with the input voltage from the microcontroller driver. The centroid of the disk was tracked with image processing program in MATLAB™. The choice of black disk was to create a good contrast between the disk and background so as to make image processing simpler. The images at each frame were cropped, segmented, and analyzed. Figure 11(*a*) illustrates the time domain response of smiling. Figures 11(*b*) and 11(*c*) show the physical appearance of smiling before and after the action unit was activated.

The jaw movement was measured similar to the face characterization described previously. Figures 12(*a*) and 12(*b*) illustrate the technique for the measurement of the jaw movement. Figure 13 shows the resulting angular movement for a square pulse with 2 s duration. The period of activation was according to the sequence derived from the facial activation code discussed in Sec. 4. This period can be programmed as required but the aim of this section is to quantify the jaw movement and the associated dynamics, which satisfies the overall goal of mimicking the jaw movement. From Fig. 13, it can be inferred that the jaw moves down by an angle of 5 deg at the beginning of the pulse and exponentially decays once the activation is stopped and then returns back to its original position

Finally, the robotic head was mounted on dynamic anthropomorphic robot with intelligence (DARwIn), a miniature humanoid robot capable of bipedal walking and performing human like motions. DARwIn version III is 600 mm tall, 4 kg robot with 21DOFs, where each joint is actuated by dc motors and utilizes a distributed control strategy. DARwIn can implement humanlike gaits while navigating obstacles and complex behaviors such as playing soccer [46–49]. A LABVIEW program for nodding and tilting was tested with a frequency of 0.25 Hz and 20 varying amplitudes of servo position. Humanlike nodding and turning was observed and quantified using the video images. Figure 14 shows the tilting and the nodding motions of the head. The side view of actuation mimics similar nodding gesture.

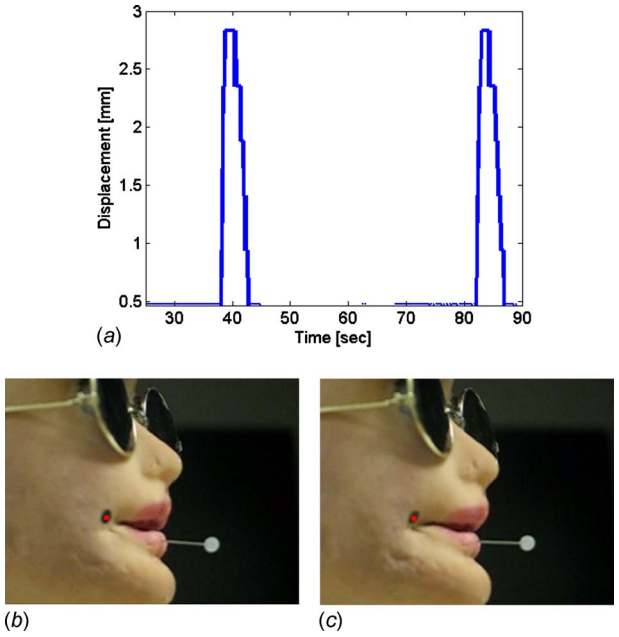

Fig. 11 Face movement characterization, (*a*) displacement response for two period activation, (*b*) before smiling action unit (AU4L) is activated, and (*c*) after AU4L is activated

Instead of walking using the static stability criterion by keeping the center of mass of its body over the support polygon by adjusting its pose of its body very slowly to minimize dynamic effects, DARwIn walks dynamically by maintaining a dynamic stability using the zero moment point (ZMP) control. ZMP is a point defined as "the point where the influence of all forces acting on the mechanism can be replaced by one single force" without a moment term [50].

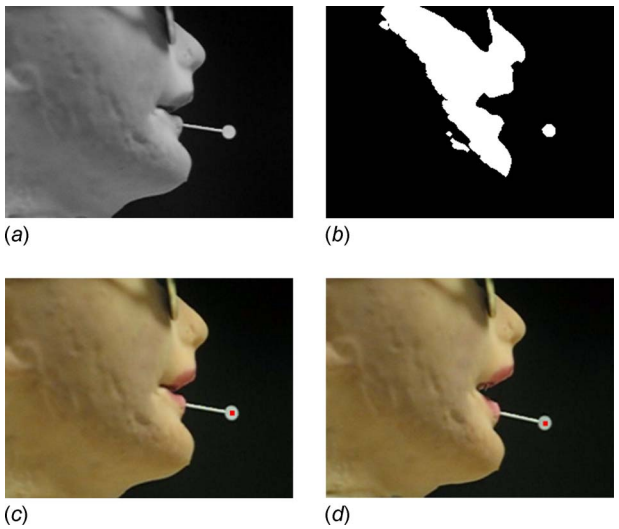

Fig. 12 (*a*) Gray scale image of the face, (*b*) object identification with dark value 100 amplitude, (*c*) normal position of the mouth with centroid tracking, and (*d*) mouth opening when jaw was activated (AU10)

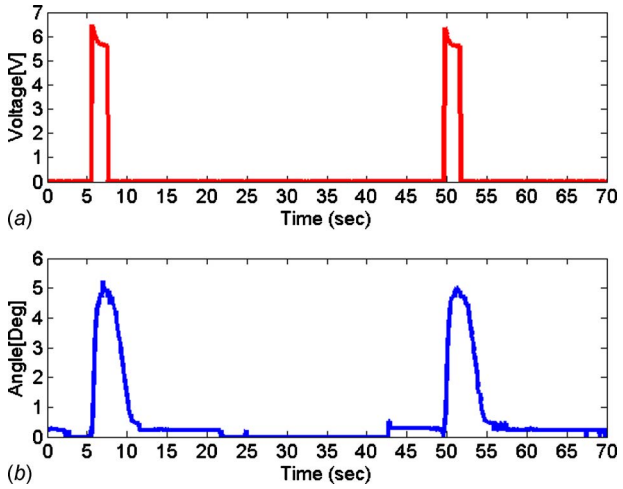

Fig. 13 Measurement and characterization of the jaw movement: (*a*) pictures of circular disk mounted on the lip, (*b*) cropped image after processing, and (*c*) jaw response for a square wave with 2 s activation and 6 V amplitude

If the ZMP remains in the support polygon, the robot can apply some force or torque to the ground to have some control over the motion of itself. However, once the ZMP moves to the edge of the foot, the robot becomes unstable and can do nothing to recover from a fall without extending the support polygon (planting another foot or arm). DARwIn uses feedback from the inertial measurement unit (IMU) to adjust the waist and arms motions to keep the ZMP inside the foot area to maintain dynamic balance [48,49]. With the new robotic head mounted, DARwIn could also use the head together with the waist and arms to control the ZMP location; however, implementation for this is left as future work.

6 Dynamic Modeling

6.1 Dynamic Modeling of Skin-SMA Configuration. The modeling of baby head includes the determination of length of SMA wire from the architecture of the head system, constitutive relationship of SMA, dynamics, and heat transfer. Figure 15 shows the arrangement of the mechanical system, SMA wire configuration, and their confinement within the skull. The AUs represented by a dot mark are attached to the SMA wire after passing over a series of pulleys and anchored at the back of the head. Such design of robotic head enables the replacement of actuators in case of any damage or loss of performance of actuator occurs. Each action unit passes through three or four pulleys. Typical pulley configuration for Au3 is shown in Fig. 15. The origin of action unit attached to the skin from the reference coordinate is indicated as *Au*. Ignoring the curvature, the vector location of each pulley is represented by *A*-*D*. The end point of the actuator securely fixed at the back side of the head is indicated as *An*. Therefore, the total length of the SMA actuator can be obtained from the vector sum as follows:

$$L = \|Au - A\| + \|B - A\| + \|C - B\| + \|D - C\| + \|An - D\| \quad (5)$$

To fully account for the total length of the SMA wrapped around the pulley, additional length factor on the sector of pulley can be included in overall length as follows:

$$L_a = L + \frac{r\pi}{180}(\theta_A + \theta_B + \theta_C + \theta_D) \quad (6)$$

where θ_i refers to the sector angle in contact with the pulley. It should be noted here that the minimum bend radius of SMA actuator should not be less than 6 mm. The SMA actuator configuration for most of the action unit is as described in Sec. 5, where the linear contraction of the actuator is attached to the skin at one end point. The other configuration of SMA actuator implemented in the jaw mechanism utilizes a lever arm mechanism.

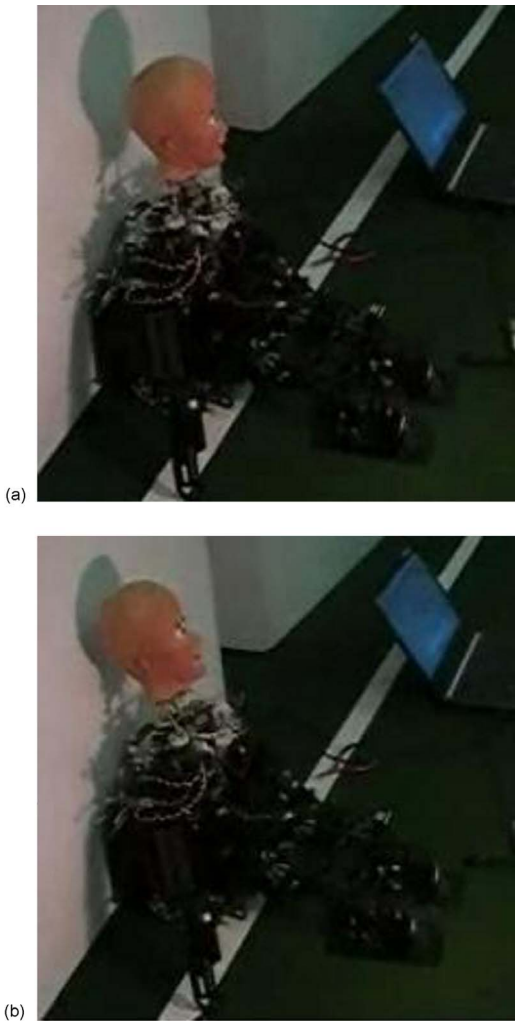

Fig. 14 Nodding of the head mounted on biped DARwIn. ((*a*) and (*b*)) Nodding gesture motion.

The general one dimensional governing equation for SMA actuator can be obtained from the constitutive relationship as

$$\sigma - \sigma_0 = E(\varepsilon - \varepsilon_0) + \Omega(\xi - \xi_0) + \vartheta(T - T_o) \quad (7)$$

where σ, ε, ξ, and T represent the stress, strain, fraction of martensite, and temperature in the SMA actuator, respectively. The respective subscript in each symbol represents the initial condition, E is the Young's modulus, ϑ is the temperature expansion coefficient, and Ω is the transformation coefficient of the material, which can be determined from the hysteresis loop of SMA ($\Omega = E\varepsilon_l$). The fraction of martensite ranges between 0 and 1 ($\xi=1$ for the martensitic phase and $\xi=0$ for the austenitic phase). The average value of the modulus of elasticity for austenite and martensite in SMA modeling provides a close approximation [51,52]. In another scenario, the modulus of the elasticity of SMA actuator is dependent on the fraction of martensite and varies as the internal temperature state changes in time [53]. The change in modulus can be written as

$$E(\xi) = E_a + \xi(E_m - E_a) \quad \text{variable modulus} \quad (8a)$$

$$E = 0.5(E_a + E_m) \quad \text{constant modulus} \quad (8b)$$

The fraction martensite is a function of transition temperature and can be obtained from the kinetic law. The four characteristic tem-

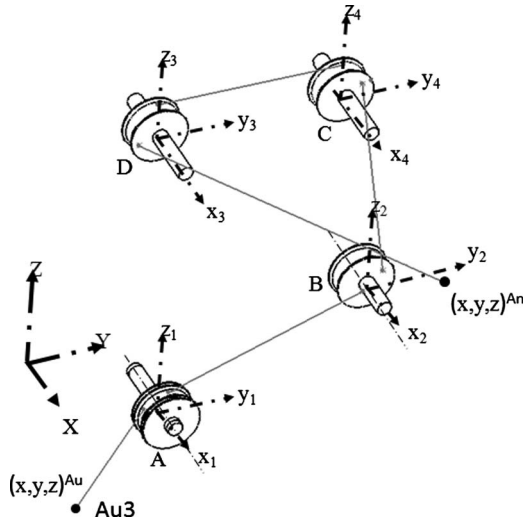

Fig. 15 Schematic diagram of pulley system and SMA actuator. (Note that Au represents action unit.)

peratures, martensite start (M_s), martensite finish (M_f), austenite start (A_s), and austenite finish (A_f), are dependent on the stress level. Considering the austenite-martensite and martensite-austenite transformations as harmonic functions of cosines, the fraction of martensite with nonzero stress state can be expressed as [54]

$$\xi_{M-A} = \frac{1}{2}\left\{\cos\left[a_A(T - A_s) - \frac{a_A}{C_A}\sigma\right] + 1\right\} \tag{9a}$$

where $a_A = \pi/(A_f - A_s)$,

$$\xi_{A-M} = \frac{1}{2}\left\{\cos\left[a_M(T - M_f) - \frac{a_M}{C_M}\sigma\right] + 1\right\} \tag{9b}$$

where $a_M = \pi/(M_s - M_f)$.

The condition for the switching martensite fraction function, according to the enhanced phenomenological model [55,56], is dependent upon the stress, the temperature, and the rate form of stress and temperature in the SMA. The condition can be written as follows:

In martensitic phase,

$$\text{if } A_s < T - \frac{\sigma}{C_A} < A_f \quad \text{and} \quad \dot{T} - \frac{\dot{\sigma}}{C_A} > 0 \tag{10a}$$

In austensitic phase,

$$\text{if } M_f < T - \frac{\sigma}{C_A} < M_s \quad \text{and} \quad \dot{T} - \frac{\dot{\sigma}}{C_A} < 0 \tag{10b}$$

The slope of stress and transformation temperature, sometimes called the stress influence coefficient, provides the value of C_A and C_M, which correspond to the austenite and martensite, respectively. The rate form of the constitutive relationship of SMA actuator can be obtained by taking the first derivative of Eqs. (7) and (9) and given by

$$\dot{\sigma} = (\dot{E})(\varepsilon - \varepsilon_0) + (E)(\dot{\varepsilon}) + (\dot{\Omega})(\xi - \xi_0) + (\Omega)(\dot{\xi}) + \dot{\vartheta}(T - T_o) + \vartheta(\dot{T}) \tag{11}$$

$$\dot{\xi}_{M-A} = -\frac{1}{2}\left\{\sin\left[a_A(T - A_s) - \frac{a_A}{C_A}\sigma\right]\right\}\left\{(a_A)(\dot{T}) - \frac{a_A}{C_A}\dot{\sigma}\right\} \tag{12a}$$

$$\dot{\xi}_{A-M} = -\frac{1}{2}\left\{\sin\left[a_M(T - M_f) - \frac{a_M}{C_M}\sigma\right]\right\}\left\{(a_M)(\dot{T}) - \frac{a_M}{C_M}\dot{\sigma}\right\} \tag{12b}$$

Usually, the input to SMA wire is provided through a recommended amount of voltage depending on the length. The governing differential equation of lumped capacitance heat transfer is obtained as

$$\dot{T} = \frac{1}{(mC_p)}\left[\frac{V^2}{R} - hA_c(T - T_\infty)\right] \tag{13}$$

where m is the mass of the actuator, h is the convective heat transfer coefficient, C_p is the specific heat capacity of the SMA alloy, V is the input voltage, A_c is the surface area of the SMA actuator, T is the temperature of the wire, and T_∞ is the ambient temperature.

Equations (11) and (13) are coupled and cannot be solved explicitly. However, the equations can be solved numerically. SIMULINK™ block diagrams were created to simultaneously obtain the state vector (stress, strain, fraction of martensite, input voltage, and temperature) for both skin actuation as well as jaw movement.

6.2 Dynamic Modeling of Jaw Mechanism: Pivoting Type Configuration. Human jaw consists of upper and lower sections known as maxillary and mandible bone. The function of jaw is to hold teeth and close mouth cavity during chewing. Jaw muscles include masseter, temporalis, medial pterygoid, and lateral pterygoid muscles whose purpose is to elevate mandible (close jaw). Lateral pterygoid and digastrics muscles are responsible for opening the mandible (open jaw) [57]. The biomechanics of human mandible and the temporomandibular joint is complex. The natural arrangement of the joint and mandible geometry allows the mandible to move in six degrees of freedom [58]. In most human being, lines drawn from the contact points of the mandibular central incisors (or the median line of the residual ridge of the mandible) to the condyle on either side form an equilateral triangle with 4 in. (102 mm) side length. The triangle is known as Bonwill triangles [59]. The triangle might not be equilateral in all human being but holds similarity in most cases [60].

For the head developed in this paper, the mandibular movement is purely rotational type about a horizontal axis. Therefore, the protruded structures on the lower jaw serve as center of rotation (*condyles*). The location of this structure, as shown in Fig. 16, is decided to be at the corner of the jaw leaving 3–4 mm thickness to that of the skull thickness. The Bonwill triangles are not replicated in this prototype: however, it mimics the mandibular rotation, which is shown in Fig. 17 as $\Delta\theta$. The two pulleys (the lowest pulley in Fig. 2) responsible for opening the jaw movement are located in the neck and its position is chosen to create maximum moment about the rotation axis J-J (Fig. 16).

Facial expression often involves wide opening of the mouth. The jaw mechanism utilizes two pairs of SMA anchored at the bottom of the lower jaw and creates a pivoting action about horizontal plane by rolling over pulleys. The isometric view of the jaw mechanism along with the local coordinate of each pulley is shown in Fig. 16(*a*). The front and top views of the jaw mechanism along with the routing pulleys are also shown in Figs. 16(*b*) and 16(*d*), respectively. The isometric view is shown in Fig. 16(*c*).

To model the mouth opening, a free body diagram of the jaw mechanism was constructed, as shown in Fig. 17. The rigid body model was developed following the principles of dynamics. The action and reaction forces, i.e., spring force (F_s), weight (W_j), and SMA torque (T_{sma}) that creates pivoting action about point O are depicted in the figure along with geometrical parameters. The line *ao* is the original position of the anchor point and *bo* after it has rotated by θ degree. The red lines represent the SMA wires. From the free body diagram shown in Fig. 17, the equilibrium condition for the torque is given as

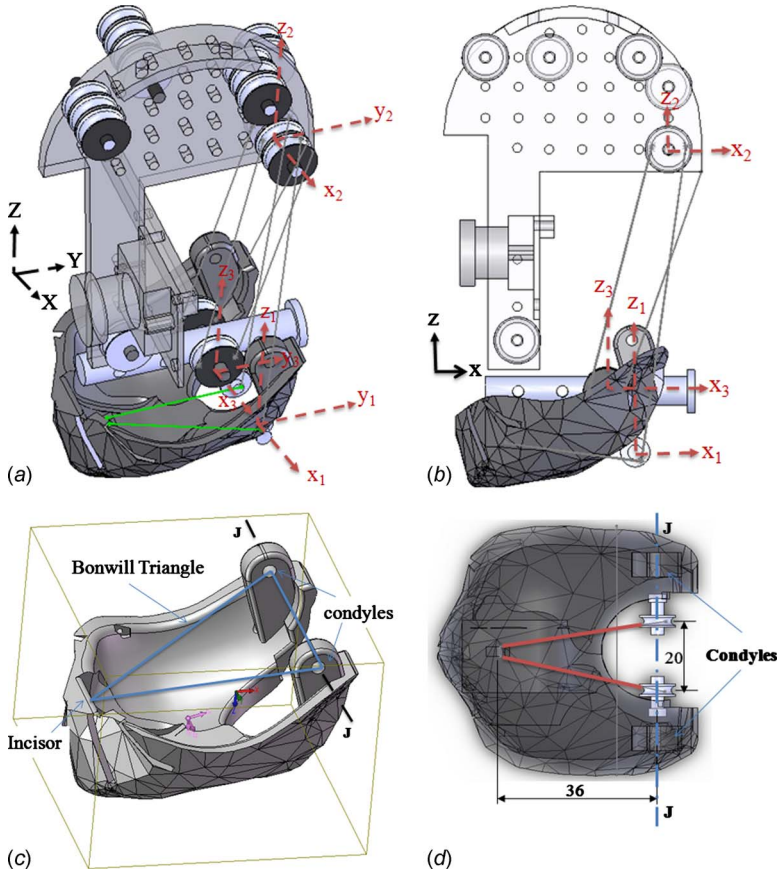

Fig. 16 Jaw mechanism: (*a*) isometric view of jaw-SMA routing pulley, (*b*) frontal view indicating local coordinates of pulleys, (*c*) isometric view of jaw, and (*d*) top view

$$T_J + T_d + T_s = T_{sma} + T_w \tag{14}$$

where T_J is the angular inertia torque, T_d is the damping torque, T_s is the spring torque, T_{sma} is the torque applied by the SMA wire, and T_w is the torque due to gravity. The torque applied by the SMA actuator can be obtained from the expressions given below:

$$T_{\text{SMA}} = \sigma_{\text{SMA}} A L_{sa}(\theta) \tag{15}$$

$$L_{sa}(\theta) = R_1 \sin(\gamma) \tag{16}$$

where A is the cross-sectional area of the SMA actuator, σ_{sma} is the stress in the SMA wire, R_1 is the distance of the SMA from the pivoting point O. In the current model, R_1 was taken to be 44 mm. The angle γ ($o\hat{a}c$ or $o\hat{b}c$) was used to determine the variable moment arm of the SMA, given as

$$\gamma = \theta + \tan^{-1}\left(\frac{H - R_1 \sin(\theta)}{R_1 \cos(\theta)}\right) \tag{17}$$

where H is the height from the pivoting point to the fixed pulley (H=32 mm). The initial angle γ_o can be obtained by setting the angle $\theta = \theta_o$. L_{SMA} is the length of the SMA actuator, and ε is the strain in the SMA. The torque due to weight can be obtained from the expression

$$T_w = mgL_w(\theta) = mgR_2 \cos(\theta) \tag{18}$$

where m is the mass of the jaw, g is the gravitational acceleration, $L_w(\theta)$ is the arm length of the weight from the pivoting point, and R_2 is the distance of the centroid to the pivoting point O (R_2 =33 mm). The spring force F_s is a function of position angle and spring stiffness that holds the jaw in the closed state during neutral position. The spring force can be expressed as

$$T_s = F_s(\theta) L_{sp}(\theta) = 2KR_3 \sin\left(\frac{\theta - \theta_0}{2}\right) R_3 \sin(\phi) \tag{19}$$

where K is the spring stiffness of the coil spring, R_3 is the distance of the end of the spring from the pivoting point O (R_3=34 mm), θ is the rotation angle from the horizontal axis, θ_o is the initial angle at neutral position, and ϕ is the angle between the action line of the spring and the arm length R_3 at any angle θ. Considering triangle Δdfo, the angle ϕ can be obtained as

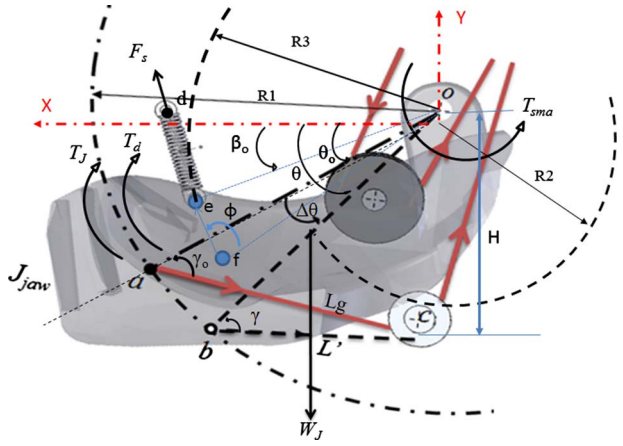

Fig. 17 Free body diagram of SMA actuated jaw

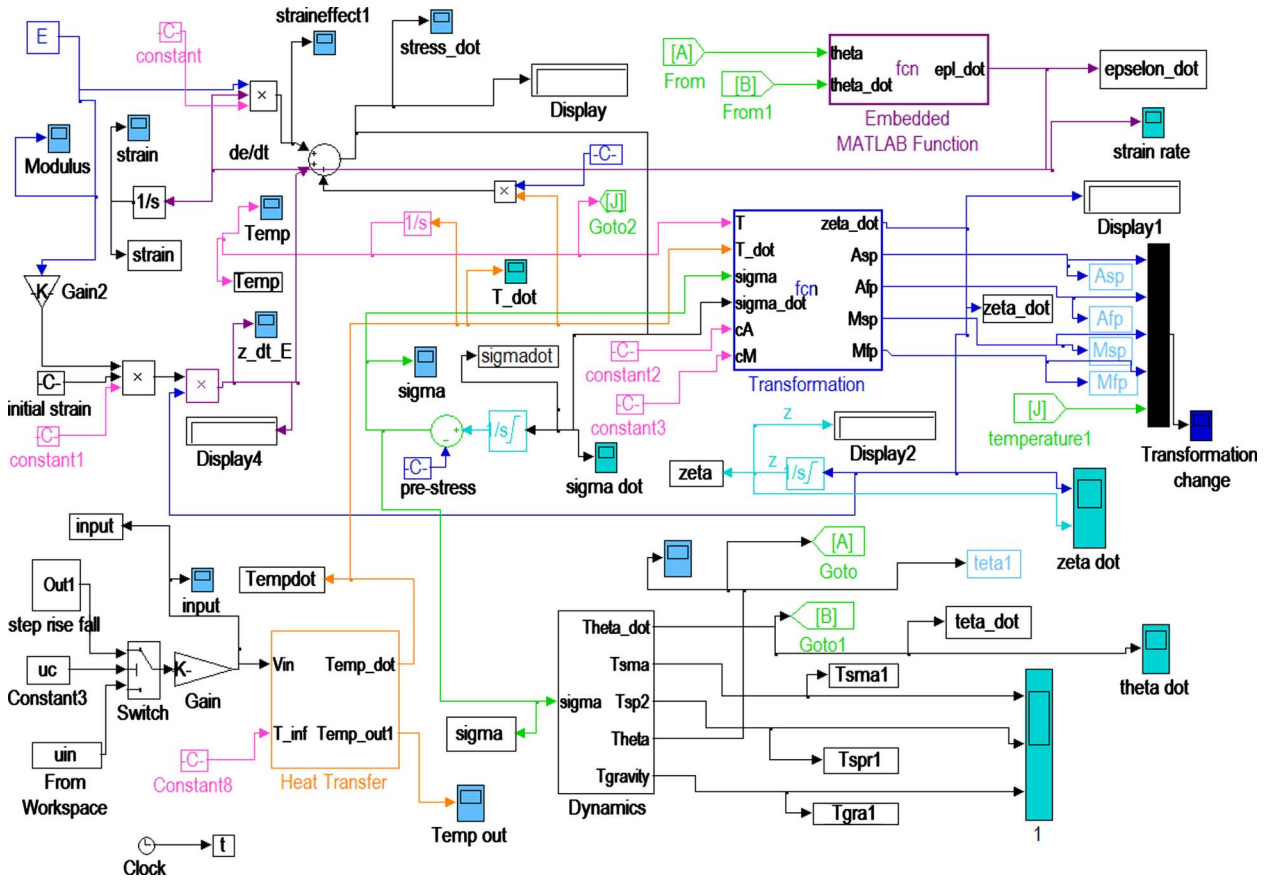

Fig. 18 SIMULINK **model of SMA actuated jaw with constant modulus**

$$\sin\phi = \frac{do}{df}\sin\beta \tag{20}$$

The initial spring rotation angle with respect to the pivoting axis is β_0 (for the current model $\beta_0 = 30$ deg). Since the rotation is a complete rigid body motion, we can obtain the following relation:

$$\beta = \theta - \theta_0 + \beta_0 \tag{21}$$

$$df = \sqrt{(do^2 + R_3^2 - 2R_3 \times do \times \cos\beta)} \tag{22}$$

where do and R_3 are fixed length ($do = 36$ mm and $R_3 = 34$ mm in the current jaw mechanism). Equation (14) can be written in terms of the angular motion of the jaw rotation about a pivoting point O and given as

$$J_{\text{jaw}}\ddot{\theta} + C\dot{\theta} + F_s(\theta)L_{sp}(\theta) = \sigma_{sma}AL_{sa}(\theta) + mgL_w(\theta) \tag{23}$$

where J_{jaw} is the polar moment of inertia of the jaw. The geometry of the lower jaw is complicated and difficult to estimate from the integral equation. However, the initial estimated value can be determined from the CAD model. Here C is the damping coefficient of the system during jaw movement, $F_s(\theta)$ is the spring force of the jaw, which is dependent on the position angle θ, σ_{SMA} is the stress in the SMA wire, A is the cross-sectional area of the SMA wire, and $L_{sa}(\theta)$ is the arm length for the SMA wire from the pivoting point. The arm length $L(\theta)$ is also a function of θ. The strain in the SMA wire can be calculated from the derivative of length L_g and given by

$$\dot{\varepsilon} = \frac{R_1\dot{\theta}\cos(\theta)\{(H - R_1\sin(\theta)) + R_1\sin(\theta)\}}{L_{\text{SMA}}\sqrt{((H - R_1\sin(\theta))^2 + (R_1\cos(\theta))^2)}} \tag{24}$$

7 SIMULINK Model

The numerical simulation of the equations described in Sec. 7 was implemented in MATLAB/SIMULINK. The block diagram is shown in Fig. 18. In this diagram, input block supplies voltage to heat transfer block, which converts it into temperature differential ($\dot{T}$). The rate of temperature change or temperature differential is provided to the phase transformation block and constitutive relationship sum block. The constitutive blocks determine the martensite fraction depending upon the stress, stress rate, temperature, and temperature rate by using a switching function. The stress rate output from the constitutive block is provided to the skin-SMA relationship. The transformation temperatures are taken out as state variables from the constitutive block indicated as A_{sp}, A_{fp}, M_{sp}, and M_{fp}. The advantage of overlaying the parameters in this manner is that all the desired state variables can be easily quantified. The integration was done using the fourth order Runge–Kutta ODE45 with variable step size. For the pivoting mechanism utilized in the jaw, the SIMULINK block diagram remains the same except for the skin-SMA block. The skin-SMA block is replaced by a dynamic block, which includes all the dynamic equations described in the dynamic modeling (Eqs. (14)–(24)). Using the SIMULINK model, the effect of various parameters such as torque due spring, SMA, gravity, inertia effect, and damping effect can be obtained.

8 Numerical Simulation

Numerical simulation is a useful tool for fundamental research to study parametric change of variables in the design process of a physical system. For SMA actuated head presented in this paper, the mathematical equations are highly nonlinear and coupled. There is no explicit mathematical solution to the coupled equations of the phase transformation, heat transfer, constitutive relation, and second order dynamic equation of motions. Therefore,

Table 3 Simulation parameter for SMA wire and baby head

Parameter	Magnitude	Unit	Reference
Diameter of SMA wire	$d=127\times10^{-6}$	(m)	[2]
Length of SMA	$L=275\times10^{-3}$ variable	(m)	Measured
Density of SMA	$\rho=6.45\times10^{3}$	(kg/m^3)	[2]
Resistivity of SMA wire	$ro=70$	(Ω/m)	[2]
Specific heat capacity	$C_p=320$	(J/kg K)	[2]
Convective heat transfer coefficient (free)	$h=120$,[a] 35,[b] 48,[c] 10, 52.8[d]	(W/m^2 °C)	[51], [61], [63], [64], [65]
Mass of SMA	$m=\rho\times\pi\times d^2\times L/4$; ($m=2.2457\times10^{-5}$)	(kg)	Calculated
Area circumference	$A_c=\pi\times d\times L$; ($A_c=1.097\times10^{-4}$)	(m^2)	Calculated
Resistance	$R=ro\times L$; ($R=19.25$)	(Ω)	[2]
Initial temperature; ambient temperature	$T_{\text{ini}}=20$; $T_{\text{inf}}=20$	(°C)	Measured
Thermal expansion coefficient	$T_{ec}=-0.055, 0.55\times10^{6}, -0.055\times10^{6}, -11\times10^{-6}, 6$ $\times10^{-6}$	(Pa/°C)	[51], [55], [62], [63], [66]
Modulus of austenite	$E_a=75\times10^{9}$;	(Pa)	[2]
Modulus of martensite	$E_m=28\times10^{9}$	(Pa)	[2]
Transformation temperature			
Austenite start	$A_s=88$	(°C)	[2]
Austenite finish	$A_f=98$	(°C)	[2]
Martensite start	$M_s=72$	(°C)	[2]
Martensite finish	$M_f=62$	(°C)	[2]
Stress influence coefficient austenite	$C_A=10$, 8,[e] 6.89[f]	(MPa/°C)	[51], [56], [61]
Stress influence coefficient martensite	$C_M=10$, 12,[e] 6.89[f]	(MPa/°C)	[51], [56], [61]
Elastomeric skin			
Skin elasticity	K_{st}=[46 57 74 89 130] [g]	(N/m)	Measured
Input voltage (step input)	$V=4.8$	(V)	-
Dynamics of the jaw			
Gravity radius	$R_2=33\times10^{-3}$	(m)	CAD
Spring radius	$R_3=34\times10^{-3}$	(m)	CAD
Inertia radius	$R_1=44\times10^{-3}$	(m)	CAD
Length of fixed position	$do=36\times10^{-3}$	(m)	CAD
Length of SMA to first pulley	$L_g=36\times10^{-3}$	(m)	CAD
Vertical height fixed	$h_l=36\times10^{-3}$	(m)	CAD
Polar moment of inertia	$I_e=17.4\times10^{-6}$	(kg m^2)	CAD
Damping coefficient	$C=0.016$, 0.02,[h] 0.025, 2	(kg m/s)	[66] and estimated
Mass of jaw	$M_j=0.017$ (from CAD); $M_j=0.0128$ (measured)	(kg)	CAD and measured
Initial angular velocity	$d(\theta_0)/dt=0$	(rad/s)	Assumed
Initial angle	$\theta_0=40\pi/180$	(rad)	CAD
Initial angle of the spring end	$\beta_0=30\pi/180$	(rad)	CAD
Spring constant supporting jaw	K=[210 280]	(N/m)	Measured

[a]Convective heat transfer of SMA actuator ($A=4.712\times10^{-4}$) used for robotic manipulator in open air environment.
[b]SMA (Ti51 at % Ni).
[c]First order term approximation.
[d]Free convection on 0.381 mm diameter 90°C Flexinol.
[e]0.381 mm diameter SMA wire.
[f]Low temperature SMA wire.
[g]See Fig. 6 for skin elasticity determination.
[h]Viscous friction damping of link mechanism and SMA wire.

numerical simulations were carried out by taking practical values of material constants of shape memory alloy and the dynamic system. The parameters for SMA such as diameter of wire, length, density, specific heat, resistivity, modulus of elasticity, transformation temperatures, and recommended voltage were obtained from vendors website (Dynalloy, Inc.). The stress influence coefficient C_M and C_A were obtained from the literature and range from 5–12 MPa/°C [55,56,61]. The convective heat transfer coefficient for free convection ranges from 10–120 W/m^2 °C [61–63]. This parameter is typically dependent on environmental conditions, whether the actuator is in horizontal or vertical configuration, and air flow velocity and for forced convection it ranges up to 300–2800 W/m^2 °C [10]. Dynamic parameters of the jaw were obtained from the computer CAD model. Damping coefficient was estimated and varied in the simulation. Summary of the simulation parameters are shown in Table 3.

9 Numerical Results and Discussion

For the simple skin-SMA relationship, the same values of stiffness of the elastomeric skin (K_{st}) for each action unit were used. It was found that as the stiffness of the skin decreases, the hysteresis loop moves to the left. In other words, lower temperature is required for phase transformation and hence to achieve 4% strain. As the stiffness of the skin increases, the SMA actuator produces larger stress with a higher slope and reaches 4% strain. Figure 19 presents several simulation results obtained from the SIMULINK model. For various magnitude of damping constant shown in Fig. 19(*a*), the strain versus temperature curve shows the hysteresis loop in the range of transformation temperature 60–100°C. As the damping factor is increased from 0.01 to 0.4, the strain reaches 4% during the heating phase for all damping factor and during the cooling phase it remains between 0.3% and 1.5% strain. The ro-

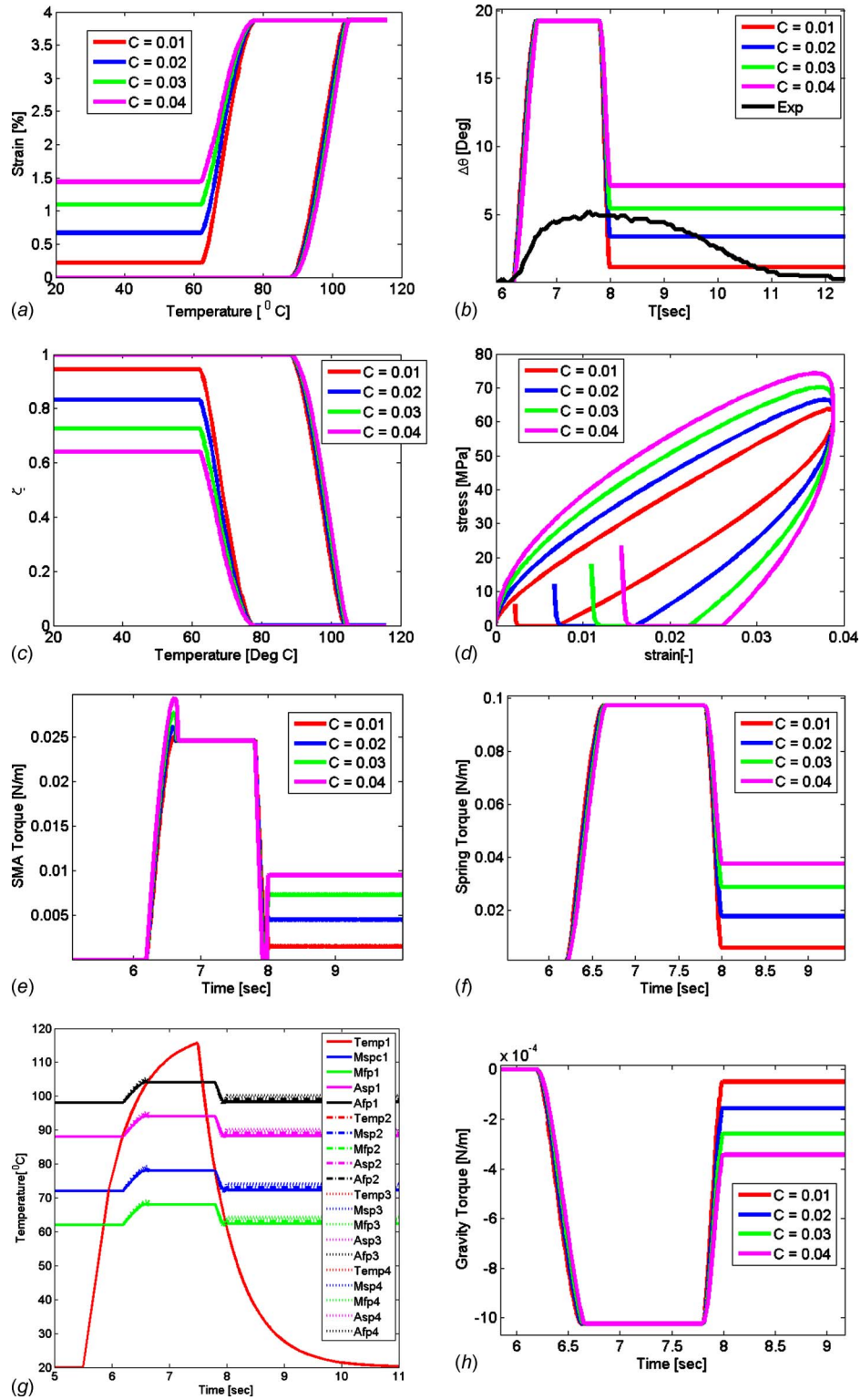

Fig. 19 Numerical results constant modulus modeling of SMA actuatored jaw. (*a*) Strain versus temperature,(*b*) angular movement, (*c*) fraction of martensite versus temperature, (*d*) stress-strain, (*e*) torque due to SMA, (*f*) torque due to spring, (*g*) temperature states, and (*h*) torque due to gravity. (T_{ec}=−11×10^{-6} Pa/°C; C_A=10.3×10^6 MPa/°C; C_A=10.3×10^6 MPa/°C; C_p =320 J/kg °C; h=110; K_s=270 N/m; M_j=0.0128 kg; I_e=1∗9.88×10^6 kg m^2; initial stress=0; and V=4.8 V amplitude square wave 2 s pulse period.)

tation angle results are shown in Fig. 19(*b*) where the total magnitude rises up to 18 deg for the magnitude of gain used for the simulation and similar to the strain response the angles return toward zero during the cooling phase but remains above 0 deg. The martensite fraction curve is also shown in Fig. 19(*c*) where the damping coefficient of 0.04 was observed in the cooling phase. The stress-strain curve shown in Fig. 19(*d*) demonstrates the shape memory effect where the strain reaches 4% during heat-

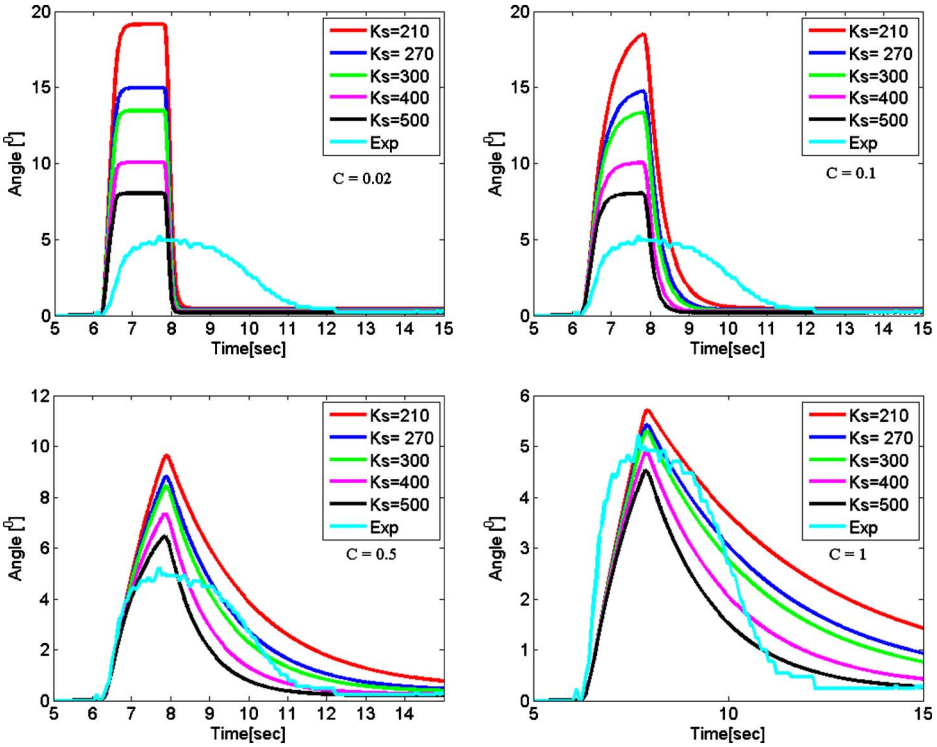

Fig. 20 Numerical and experiment angles of jaw movement for a 50 MPa step stress input to the dynamic block

ing and returns back to zero stress during cooling with a certain slope. Figure 19(*e*) illustrates the torque only due to the SMA; in this case, the magnitude of torque reaches steady state at 0.025 N m of all damping except for 0.04 damping factor where a hump at the beginning is observed. Note that four SMA actuators are pulling the jaw to open the mouth and each SMA is assumed to contribute the same amount of stress and hence the same torque. Figure 19(*f*) shows the spring torque where the magnitude reaches 0.1 N m for all damping during the heating and exhibits different steady state torques during cooling. All the transformation temperatures, M_s, M_f, A_s, and A_f, for all damping cases are shown in Fig. 19(*g*). In this case, the damping did not significantly affect the profile of the transformation temperature. The temperature state of the wire is shown in red solid line, which crosses the four stress-induced transition temperatures $(M_{sp}, M_{fp}, A_{sp}, A_{fp})$, reaches 110°C, and exponentially decays according to the time constant of the heat transformation equation. The time constant is a function of specific heat capacity (C_p), convective heat transfer coefficient (h), mass of the actuator (m), and surface area of the actuator (A_c). It can be obtained from Eq. (9) and given as $=hA_s/mC_p$. The torque due to gravity is shown in Fig. 19(*h*) and the magnitude of the torque is in the range of 0.001 N m, which is relatively lower than the torque due to SMA and the spring. By considering its magnitude, the torque due to gravity may be ignored during the modeling of the system described here. The numerical simulation shown in Fig. 19(*b*) underestimates the experimental measured angle for the value of stiffness and damping coefficient considered. The prime goal of the simulation result in Fig. 19 is to provide an insight to all state variables, which determine the performance. The simulation result can be tuned by taking accurate measurement of SMA material properties and simulation parameter listed in Table 3. The dynamic performance of jaw movement can be further be investigated by considering only the dynamic block model and providing step input stress. The operating point of jaw motion is around 2.5 N (50 MPa in each SMA). Therefore, simulations were carried out by providing 50 MPa step input stress and assuming the four numbers of SMA actuator create additive effects in moving the jaw. The damping coefficient assumed in simulation significantly affects the response time. Assuming a linear spring, the variation of spring stiffness, which includes the elasticity of skin material covering the artificial skull, affects the steady state angle of the jaw movement. Therefore, numerical simulations were carried out by varying the spring stiffness K_s and damping. The measured angle and simulation result are shown in Fig. 20. It can be seen in Fig. 20(*a*) that a measured spring constant value and low damping did not provide the profile of jaw movement. However, for higher damping value and a range of stiffness, the jaw movement numerical simulation and experimental results follow similar profile and amplitude.

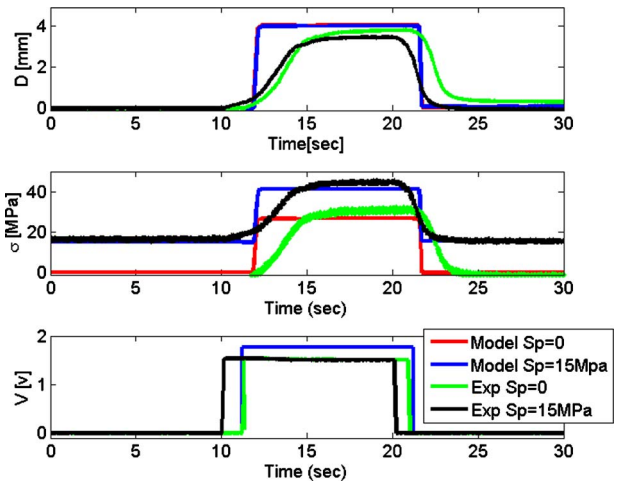

Fig. 21 Numerical and experimental results of time domain force, displacement for square wave input voltage under prestress condition (SMA wire diameter=127 μm)

Table 4 Specification of baby-DARwIn presented in this paper

Face	12DOF movement including jaw Flexinol and Biometal fiber actuators Diameter 100 μm and 127 μm Length of actuator varies from 150 mm to 360 mm
Neck	2DOF neck mechanism Servo motor HS 225 Controlled with RS 232 and LABVIEW program
Head	Overall size $140\times90\times110$ mm^3 Weight $\sim$0.5 kg
Vision system	Two firewire CMOS cameras
Body	21 DOF Maxon's RE-max coreless dc motors Distributed control strategy Height 600 mm; and weight 4 kg
Facial control system	PIC series microcontroller based custom-built driving circuit with 20 MHz clock signal and embedded code
Neck driving system	USB interfaced by Polulo controller Consumes 6 V power supply for digital electronics -6 V dc power for the servo motors
Computer interface and platform	Windows operating system and LABVIEW program and assembly language

10 Experimental Characterization

Experiment on SMA actuator under various prestress amplitudes was investigated in our previous work [10], where the actuator was connected to a bias spring mounted on a translating stage to vary the prestress amplitude and the measurement was conducted for time dependent stress and strain at a recommended input voltage. The SIMULINK model presented in Sec. 3 was compared with the experimental results. In this case, a 127 μm in diameter 90 deg Flexinol wire was selected to compare the numerical simulation. The actuator was subjected to 10 s activation with a step input voltage and the resulting stress and strain were compared. Figure 21 presents both the experimental and numerical simulation results on 127 μm Flexinol wire for prestress conditions (0 MPa and 20 MPa). From the displacement curve, the experimental values rise exponentially to 4% strain within 5 s and then decay slowly to reach the original position. The simulation result shows a sharp rise. A similar behavior was observed in the stress response plots. Both the stress and strain amplitudes are bounded by the numerical simulation result; however, the decay in the experimental result is not observed in the numerical simulation. This could be caused by the variation of estimated parameters and model simplification.

11 Conclusion

A small scale biped robot that could be used for children education, entertainment, and household activities was developed in this study, focusing on facial expressions. The goal of this paper was on the mechatronic approach of developing a humanoid head using shape memory alloy wires. Humanlike facial expressions were demonstrated by combining the SMAs with the elastomeric skin, mechanical components, and microcontroller based driving electronics. A relationship among actuator parameter, skin properties, and actuation system was studied and the characterization of facial expression and gestures on humanoid platform was demonstrated. Several practical issues in humanoid head development were discussed. The unique feature of the baby head is the ability to integrate numerous actuators with their 35 routine pulleys, two firewire CMOS cameras that serve as eyes in just $140\times90\times110$ mm^3 dimension skull. The battery powered microcontroller base driving circuit for actuating all the muscles allows both standalone facial expression platform and untethered mountable head on small biped. The microcontroller was programmed in assembly language, which sequentially executes the facial emotion routine and could be programmed on demand. The humanoid baby face with 12DOFs was combined with the DARwIn robot, which has 21DOF articulated movement, resulting in a total of 33DOF system. To our knowledge, the combined baby-DARwIn is the highest degree of freedom facial expressive small humanoid biped robot. A nonlinear mathematical formulation describing the dynamic behavior of humanoid head focusing on the jaw was presented and numerical simulations along with experimental verification were presented. SIMULINK models were developed that provide inaccessible state variables, which would have required several sensors to predict the nature of physical quantities. The parametric study carried out to study the influence of system variables such as damping and stiffness provide insightful information for the optimization of the performance. Table 4 summarizes the main results and specifications.

Acknowledgment

The authors gratefully acknowledge the financial support from the Office of Naval Research (ONR) through Grant No. N000140810654 and the Institute of Critical Technology and Applied Science (ICTAS) at Virginia Tech.

References

[1] Actuator comparison, http://ndeaa.jpl.nasa.gov/nasa-nde/lommas/eap/actuators-comp.pdf
[2] Dynalloy, Inc., www.Dynalloy.com
[3] Madden, J. D. W., Vandesteeg, N. A., Anquetil, P. A., Madden, P. G. A., Takshi, A., Pytel, R. Z., Lafontaine, S. R., Wieringa, P. A., and Hunter, I. W., 2004, "Artificial Muscle Technology: Physical Principles and Naval Prospects," IEEE J. Ocean. Eng., **29**(3), pp. 706–728.
[4] Kornbluh, R., Perline, R., Eckerle, J., and Joseph, J., 1998, "Electrostrictive Polymer Artificial Muscle," Proceedings of the IEEE Robotics and Automation, Vol. 3, pp. 2147–2154.
[5] Kornbluh, R., Pelrine, R., Pei, Q., Oh, S., and Joseph, J., 2000, "Ultrahigh Strain Response of Field-Actuated Elastomeric Polymers," Proc. SPIE, **3987**,

pp. 51–64.
[6] Tadesse, Y., Grange, R. W., and Priya, S., 2009, "Synthesis and Cyclic Force Characterization of Helical Polypyrrole Actuators for Artificial Facial Muscles," Smart Mater. Struct., **18**, p. 085008.
[7] Tadesse, Y., Priya, S., Chenthamarakshan, C. R., de Tacconi, N. R., and Rajeshwar, K., 2008, "Polypyrrole–Polyvinylidene Difluoride Composite Stripe and Zigzag Actuators for Use in Facial Robotics," Smart Mater. Struct., **17**(2), p. 025001.
[8] Davis, S., and Caldwell, D. G., 2006, "Braid Effects on Contractile Range and Friction Modeling in Pneumatic Muscle Actuators," Int. J. Robot. Res., **25**(4), pp. 359–369.
[9] Tsagarkis, N., and Caldwell, D. G., 2000, "Improved Modeling and Assessment of Pneumatic Muscle Actuators," Proceedings of the IEEE, San Francisco, CA.
[10] Tadesse, Y., Thayer, N., and Priya, S., 2010, "Tailoring the Response Time of Shape Memory Alloy Wires Through Active Cooling and Pre-Stress," J. Intell. Mater. Syst. Struct., **21**(1), pp. 19–40.
[11] TOKI Corp., http://www.toki.co.jp
[12] Hanson, D., Bergs, R., Tadesse, Y., White, V., and Priya, S., 2006, "Enhancement of EAP Actuated Facial Expressions by Designed Chamber Geometry in Elastomers," Proc. SPIE, **6168**, pp. 49–57.
[13] Weiguo, W., Qingmei, M., and Yu, W., 2004, "Development of the Humanoid Head Portrait Robot System With Flexible Face and Expression," 2004 IEEE International Conference on Robotics and Biomimetics, ROBIO, pp. 757–762.
[14] Tian, Y. L., Kanade, T., and Cohn, J. F., 2001, "Recognizing Action Units for Facial Expression Analysis," IEEE Trans. Pattern Anal. Mach. Intell., **23**(2), pp. 97–115.
[15] Burrows, A. M., 2008, "The Facial Expression Musculature in Primates and Its Evolutionary Significance," BioEssays, **30**, pp. 212–225.
[16] Trezopoulos, D., and Waters, K., 1990, "Physically-Based Facial Modeling, Analysis, and Animation," Journal of Visualization and Computer Animation, **1**(2), pp.73–80.
[17] Ekman, P., and Friesen, W. V., 1978, *Facial Action Coding System*, Consulting Psychologist, Palo Alto, CA.
[18] Oh, J. H., Hanson, D., Kim, W. S., Han, Y., Kim, J. Y., and Park, I. W., 2006, "Design of Android Type Humanoid Robot Albert HUBO," IEEE/RSJ International Conference on Intelligent Robots and Systems, pp. 1428–1433.
[19] Hashimoto, T., Hitramatsu, S., Tsuji, T., and Kobayashi, H., 2006, "Development of the Face Robot SAYA for Rich Facial Expressions," SICE-ICASE International Joint Conference, pp. 5423–5428.
[20] Shimada, M., Minato, T., Itakura, S., and Ishiguro, H., 2006, "Evaluation of Android Using Unconscious Recognition," Sixth IEEE-RAS International Conference on Humanoid Robots, pp. 157–162.
[21] Guenter, F., Roos, L., Guignard, A., and Billard, A. G., 2005, "Design of a Biomimetic Upper Body for the Humanoid Robot Robota," Proceedings of the Fifth IEEE/RAS International Conference on Humanoid Robots, pp. 56–61.
[22] Berns, K., and Hirth, J., 2006 "Control of Facial Expressions of the Humanoid Robot Head ROMAN," Proceedings of the IEEE/RSJ International Conference on Intelligent Robots and Systems, pp. 3119–3124.
[23] Tadesse, Y., and Priya, S., 2008, "Humanoid Face Utilizing Rotary Actuator and Piezoelectric Sensor," Paper No. IMECE2008-66860.
[24] Solis, J., Suefuji, K., Taniguchi, K., and Takanishi, A., 2006, "Imitating the Human Flute Playing by the WF-4RII: Mechanical, Perceptual and Performance Control Systems," IEEE/RAS-EMBS International Conference on Biomedical Robotics and Biomechatronics, pp. 1024–1029.
[25] Mumolo, E., Nolich, M., and Vercelli, G., 2007, "An Interactive Receptionist Robot for Users With Vocal Pathologies," Tenth IEEE International Conference on Rehabilitation Robotics, Noordwijk, The Netherlands.
[26] Ido, J., Myouga, Y., Matsumoto, Y., and Ogasawara, T., 2003, "Interaction of Receptionist ASKA Using Vision and Speech Information," Proceedings of the IEEE International Conference on Multisensor Fusion and Integration for Intelligent Systems, pp. 335–340.
[27] Allison, B., Nejat, G., and Kao, E., 2009, "The Design of an Expressive Humanlike Socially Assistive Robot," ASME J. Mech. Rob., **1**, pp. 1–8.
[28] Hanson, D., Olney, A., Pereira, I. A., and Zielke, M., 2005, "Upending the Uncanny Valley," Proceedings of the National Conference on Artificial Intelligence.
[29] MacDorman, K. F., and Ishiguro, H., 2006, "The Uncanny Advantage of Using Androids in Cognitive and Social Science Research," *Interaction Studies*, John Benjamins, Amsterdam, pp. 297–337.
[30] Mori, M., 1970, "The Uncanny Valley," Energy, **7**(4), pp. 33–35.
[31] Breazeal, C., Gray, J., and Berlin, M., 2009, "An Embodied Cognition Approach to Mindreading Skills for Socially Intelligent Robots," Int. J. Robot. Res., **28**(5), pp. 656–680.
[32] Kobayashi, H., 2001, "A Study of Face Robot Platform as KANSEI Medium," J. Robotics Mechatronics, **13**(5), pp. 497–504.
[33] Kobayashi, H., Ichikawa, Y., Senda, M., and Shiiba, T., 2002, "Towards Rich Facial Faial Expression by Face Robot," Proceedings of the International Symposium on Micromechatronics and Human Science (MHS 2002), pp. 139–145.
[34] Hara, F., Akazawa, H., and Kobayashi, H., 2001, "Realistic Facial Expressions by SMA Driven Face Robot," Proceedings of the Tenth IEEE International Workshop on Robot and Human Interactive Communication, pp. 504–511.
[35] Tadesse, Y., Bergs, R., Priya, S., Stephanou, H., Popa, D., and Hanson, D., 2006, "Piezoelectric Actuation and Sensing for Facial Robotics," Ferroelectrics, **345**, pp. 13–25.
[36] Rossi, D., Pioggia, G., Carpi, F., Ahluwalia, A., Lorussi, F., and Rocchia, W., 2002, "Creating Facial Expressions Using Polymeric Muscles," Proceedings of the First Conference on Artificial Muscles.
[37] Tadesse, Y., Moore, D., Thayer, N., and Priya, S., 2009, "Silicone Based Artificial Skin for Humanoid Facial Expressions," Proc. SPIE, **7287**, p. 728709.
[38] Velázquez, R., Pissaloux, E., Hafez, M., and Szewczyk, J., 2005, "A Low-Cost Highly-Portable Tactile Display Based on Shape Memory Alloy Micro-Actuators," VECIMS 2005—IEEE International Conference on Virtual Environments, Human-Computer Interfaces, and Measurement Systems.
[39] Angelino, M. R., and Washington, G. N., 2002, "Design and Construction of a Piezoelectric Point Actuated Active Aperture Antenna," J. Intell. Mater. Syst. Struct., **13**, pp. 125–136.
[40] Villanueva, A., Bresser, S., Chung, S., Tadesse, Y., and Priya, S., 2009, "Jellyfish Inspired Unmanned Underwater Vehicle," Proc. SPIE, **7287**, p. 72871G.
[41] Pack, R. T., Christopher, J. L., Jr., and Kawamura, K., 1997, "A Rubbertuator-Based Structure-Climbing Inspection Robot," Proceedings of the IEEE International Conference on Robotics and Automation, Albuquerque, NM.
[42] Li, H., and Yang, S. X., 2003, "A Behavior-Based Mobile Robot With a Visual Landmark-Recognition System," IEEE/ASME Trans. Mechatron., **8**(3), pp. 476–482.
[43] Hernández, S., Torres, J. M., Morales, C. A., and Acosta, L., 2003, "A New Low Cost System for Autonomous Robot Heading and Position Localization in a Closed Area," Auton. Rob., **15**, pp. 99–110.
[44] Ruffier, F., and Franceschini, N., 2005, "Optic Flow Regulation: The Key to Aircraft Automatic Guidance," Rob. Auton. Syst., **50**, pp. 177–194.
[45] Al-Dhaher, A. H. G., 2001, "Integrating Hardware and Software for the Development of Microcontroller-Based Systems," Microprocessor and Microsystems, **25**, pp. 317–328.
[46] Hong, D. W., 2006, "Biologically Inspired Locomotion Strategies: Novel Ground Mobile Robots at RoMeLa," URAI International Conference on Ubiquitous Robots and Ambient Intelligence (URAI 2006).
[47] Muecke, K. J., and Hong, D. W., 2007, "Development of an Open Humanoid Robot Platform for Research and Autonomous Soccer Playing," 22nd AAAI Conference on Artificial Intelligence, Vancouver, BC, Canada.
[48] Muecke, M., Hong, D. W., and Lim, S., 2008, "Precision Circular Walking of Bipedal Robots," 32nd ASME Mechanisms and Robotics Conference, New York, Aug. 3–6.
[49] Muecke, M., and Hong, D. W., 2008, "The Synergistic Combination of Research, Education, and International Robot Competitions Through the Development of a Humanoid Robot," 32nd ASME Mechanisms and Robotics Conference, New York, Aug. 3–6.
[50] Vukobratovic, M., 2004, "Zero-Moment Point—Thirty Five Years of Its Life," Int. J. Humanoid Robotics, **1**(1), pp. 157–173.
[51] Elahinia, M. H., and Ashrafiuon, H., 2002, "Nonlinear Control of a Shape Memory Alloy Actuated Manipulator," Trans. ASME, **124**, pp. 566–575.
[52] Jayender, J., Patel, R. V., Nikumb, S., and Ostojic, M., 2005, "Modelling and Gain Scheduled Control of Shape Memory Alloy Actuators," Proceedings of the 2005 IEEE Conference on Control Applications, Toronto, ON, Canada.
[53] Zhu, S., and Zhang, Y., 2007, "A Thermomechanical Constitutive Model for Superelastic SMA Wire With Strain-Rate Dependence," Smart Mater. Struct., **16**, pp. 1696–1707.
[54] Leo, D. J., 2007, *Engineering Analysis of Smart Material Systems: Analysis, Design, and Control*, Wiley, New York.
[55] Elahinia, M., and Ahmadian, M., 2005, "An Enhanced SMA Phenomenological Model: I. The Shortcomings of the Existing Models," Smart Mater. Struct., **14**, pp. 1297–1308.
[56] Elahinia, M., and Ahmadian, M., 2005, "An Enhanced SMA Phenomenological Model: II. The Experimental Study," Smart Mater. Struct., **14**, pp. 1309–1319.
[57] Hertling, D., and Kessler, R., 2006, *Management of Common Musculoskeletal Disorders: Physical Therapy Principles*, Lippincott Williams & Wilkins, Philadelphia, PA.
[58] Santos, I., Tavares, J., Mendes, J., and Paulo, M., 2008, "A Prototype System for Acquisition and Analysis of 3D Mandibular Movement," Int. J. Mech. Mater. Des., **4**, pp. 173–180.
[59] Wilson, G., 1921, "The Anatomy and Physics of the Temporomandibular Joint," J. Am. Dent. Assoc., **8**, pp. 236–241.
[60] Živanović, S., 1969, "Bonwill's Triangle and Asymmetry in East African Human Mandibles," Arch. Oral Biol., **14**(9), pp. 1041–1044.
[61] Prahlad, H., and Chopra, I., 2003, "Development of a Strain-Rate Dependent Model for Uniaxial Loading of SMA Wires," J. Intell. Mater. Syst. Struct., **14**(7), pp. 429–442.
[62] Jayender, J., Patel, R. V., Nikumb, S., and Ostojic, M., 2008, "Modeling and Control of Shape Memory Alloy Actuators," IEEE Trans. Control Syst. Technol., **16**, pp. 279–287.
[63] Tabrizi, V. A., and Moallem, M., 2007, "Nonlinear Position Control of Antagonistic Shape Memory Alloy Actuators," Proceedings of the 2007 American Control Conference, New York, Jul 11–13.
[64] Luo, Y., Takagi, T., Maruyama, S., and Yamada, M., 2000, "A Shape Memory Alloy Actuator Using Peltier Modules and R-Phase Transition," J. Intell. Mater. Syst. Struct., **11**(7), pp. 503–511.
[65] Potapov, P., and Da Silva, E., 2000, "Time Response of Shape Memory Alloy Actuators," J. Intell. Mater. Syst. Struct., **11**(2), pp. 125–134.
[66] Ashrafiuon, H., Eshraghi, M., and Elahinia, M. H., 2006, "Position Control of a Three-Link Shape Memory Alloy Actuated Robot," J. Intell. Mater. Syst. Struct., **17**(5), pp. 381–392.